Geochemical Perspectives Letters

Vivianite-parasymplesite solid solution: A sink for arsenic in ferruginous environments?

J.P.H. Perez[1*], M. Okhrymenko[1,†], R. Blukis[1,‡], V. Roddatis[1], S. Mayanna[1,§], J.F.W. Mosselmans[2], L.G. Benning[1,3]

https://doi.org/10.7185/geochemlet.2325

Abstract

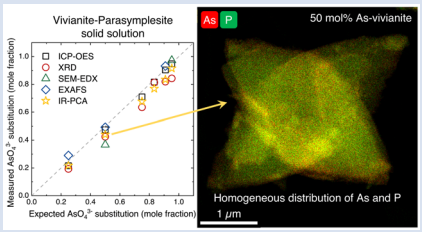

Vivianite, a hydrated ferrous phosphate [$Fe^{II}_3(PO_4)_2 \cdot 8\ H_2O$] that forms in oxygen-poor, but Fe^{2+}-rich conditions is important in nutrient cycling in anoxic environments. In natural vivianites, isomorphic substitution of divalent cations for structural Fe(II) are typical. However, anion substitution is rare; in particular, arsenate ($As^{V}O_4^{3-}$) substitution has never been documented in natural vivianites. Only partial substitution has been reported in synthetic analogues, and parasymplesite [$Fe^{II}_3(AsO_4)_2 \cdot 8\ H_2O$], the arsenic end member of the vivianite mineral group, is found in hydrothermal deposits. In this study, we detail structural changes in synthesised As-vivianites ($Fe^{II}_3[(PO_4)_{1-x}(AsO_4)_x]_2 \cdot 8\ H_2O$) with systematically increased degrees of As(V) substitution ($0.22 \leq x \leq 0.95$). As(V) was successfully incorporated into the vivianite crystal structure, creating a homogenous, solid solution between $As^{V}O_4^{3-}$ and PO_4^{3-}. Like both end members, the intermediate As-vivianites crystallised in the monoclinic system (*C*2/*m* space group), and retained the platelet crystal habit of As-free vivianite, even at the highest As(V) substitution. This uniform incorporation of As(V), and its replacement of PO_4^{3-}, provides a potentially stable sink for arsenic in anoxic soils and sediments, and may have implications in ferruginous early Earth oceans.

Received 24 January 2023 | Accepted 30 June 2023 | Published 3 August 2023

Introduction

Phosphorus is an essential nutrient that controls primary productivity in terrestrial and aquatic systems. Retention of phosphorus is strongly dependent on biomass uptake, mineral co-precipitation, or sorption onto mineral surfaces (Filippelli, 2002). In anoxic soils and sediments, reductive dissolution of Fe(III) (oxyhydr)oxides results in the release of dissolved phosphate (PO_4^{3-}) and Fe^{2+} (Patrick and Khalid, 1974), accompanied by increase to near neutral pH due to H^+ consumption (Walpersdorf *et al.*, 2013). Under anoxic, non-sulfidic (*i.e.* ferruginuous) conditions, high dissolved Fe^{2+} and PO_4^{3-} may lead to vivianite [$Fe^{II}_3(PO_4)_2 \cdot 8\ H_2O$] (Heiberg *et al.*, 2012) precipitation at near neutral pH. Vivianite can also form in aquatic ferruginous environments such as marine and lacustrine sediments and lakes (Egger *et al.*, 2015; Vuillemin *et al.*, 2020), and has been suggested as a potential phosphate sink in early Earth oceans (Hao *et al.*, 2020), affecting trace element cycling and nutrient availability.

Vivianite is the Fe(II) phosphate end member of the vivianite mineral group (monoclinic *C*2/*m*), represented by the general formula $M_3(YO_4)_2 \cdot 8\ H_2O$, where *M* refers to divalent cation(s) (*e.g.*, Fe(II), Mg, Mn) and *Y* can be either P or As. Vivianite is a poorly soluble mineral ($pK_{sp} \approx 35.8 \pm 0.08$ at 25 °C; Al-Borno and Tomson, 1994) that is stable under reducing and circum-neutral pH (6–9) conditions (Nriagu, 1972). Its structure has two crystallographically and chemically distinct Fe sites coordinated with phosphate (Fig. S-1): (i) a single octahedral Fe1 site [$Fe(H_2O)_4O_2$)], and (ii) two edge sharing octahedral Fe2 sites [$Fe_2(H_2O)_4O_6$] (Mori and Ito, 1950; Bartl, 1989). These single and double edge sharing Fe octahedra are connected by tetrahedral phosphate to form layers in (010), interconnected by hydrogen bonds between lattice water molecules.

Isomorphic substitution of Fe^{2+} by divalent cations (*e.g.*, Mg, Mn) occurs frequently in natural vivianites, and although rarely documented, anions like arsenate (AsO_4^{3-}) can also replace PO_4^{3-} in the crystal structure (Muehe *et al.*, 2016). Anion substitution is possible because of chemical and structural similarities between phosphate and arsenate (*i.e.* geometry, size, pK_a). Full substitution of phosphate for arsenate results in a new phase, parasymplesite [$Fe^{II}_3(AsO_4)_2 \cdot 8\ H_2O$]. Contrary to vivianite, parasymplesite is usually found in oxidised zones of As-rich hydrothermal mineral deposits (Anthony *et al.*, 2000). Johnston and Singer (2007), however, predicted that parasymplesite can form in near neutral pH, reduced As-impacted groundwater (*e.g.*, Bangladesh), yet it has so far not been

1. GFZ German Research Center for Geosciences, Telegrafenberg, 14473 Potsdam, Germany
2. Diamond Light Source, Harwell Science and Innovation Campus, Didcot, Oxfordshire, OX11 0DE, United Kingdom
3. Department of Earth Sciences, Freie Universität Berlin, Malteserstrasse 74-100, 12249 Berlin, Germany
† Current affiliation: Department of Chemistry, RWTH Aachen University, 52056 Aachen, Germany
‡ Current affiliation: Leibniz-Institut für Kristallzüchtung (IKZ), Berlin 12489, Germany
§ Current affiliation: Carl Zeiss Microscopy GmbH, 73447 Oberkochen, Germany
* Corresponding author (Email: jpperez@gfz-potsdam.de)

reported. As(V)-substituted vivianite (~15 mol %; hereafter referred as As-vivianite) have been observed during microbial reduction of As(V)-bearing Fe(III) (oxyhydr)oxides (Muehe *et al.*, 2016), and such high As contents suggest a possible vivianite-parasymplesite solid solution. Thus, it is possible that As-vivianites are unrecognised possible host minerals and sinks for As in many anoxic environments.

To test this, we synthesised As-vivianites ($Fe_3[(PO_4)_{1-x}(AsO_4)_x]_2 \cdot 8\,H_2O$), with increasing degrees of AsO_4^{3-} substitution ($0.22 \leq x \leq 0.95$), under anoxic and near neutral pH conditions. Our results will help us better understand As dynamics in oxygen limited, Fe^{2+}-rich environments. We show that a continuous solid solution between vivianite and parasymplesite exist, and document how the structure, morphology and bonding environment of As-vivianite changes with increasing As(V) substitution. We also discuss how such a solid solution mineral system can be important in modern and ancient ferruginous, or contaminated environmental settings.

Materials and Methods

Co-precipitation experiments were conducted at room temperature in acid cleaned 120 mL perfluoroalkoxy (PFA) jars inside a vinyl-walled glovebox (97 % N_2, 3 % H_2). Stock solutions were prepared using deoxygenated ultrapure water (resistivity ~18.2 MΩ·cm), obtained by purging with argon at 90 °C for ~4 hr. Aliquots from stock solutions of 20 mM Na_2HAsO_4 and 20 mM Na_2HPO_4 (pH ~ 7) were mixed with ultrapure water to achieve desired AsO_4^{3-} mole fractions of 0.25, 0.50, 0.75, 0.83, 0.91 and 0.95 ($[AsO_4^{3-} + PO_4^{3-}] = 8$ mM). These were mixed with an aliquot of 0.58 M $Fe^{II}SO_4$ stock solution to achieve an $[Fe^{2+}]/[AsO_4^{3-} + PO_4^{3-}]$ ratio of 1.5 and pH ≈ 5. Precipitation was triggered by dropwise addition of 1 M NaOH, while stirring until pH 7.1 ± 0.2 was reached. Mineral suspensions were aged for 1 and 24 hr under constant stirring. End members, vivianite (no AsO_4^{3-}) and parasymplesite (no PO_4^{3-}) were also synthesised under similar conditions. Solids were collected by filtration, washed with deoxygenated ultrapure water, and subsequently dried, ground and stored in the glovebox until characterisation. The solutions and solids were characterised using inductively coupled plasma optical emission spectrometry (ICP-OES), powder X-ray diffraction (XRD), scanning and transmission electron microscopy (S/TEM), synchrotron-based X-ray absorption spectroscopy (XAS) and Fourier transform infrared (FTIR) spectroscopy. Detailed information on all characterisation methods and geochemical modelling can be found in Supplementary Text S-2.

Results and Discussion

Structure and composition of As-vivianites. The precipitates after 1 and 24 hr of aging were highly crystalline (Figs. 1a, S-2). All Bragg reflections could be assigned to vivianite or parasymplesite with no observable peak splitting, indicating homogeneity of the precipitates. No other crystalline Fe-P or Fe-As phases were present, and the similarity in the backgrounds in all patterns also suggest the lack of any amorphous phase contribution. The XRD results agree with our geochemical calculations (see saturation indices in Table S-2), which showed that vivianite and parasymplesite are the only thermodynamically stable phases in our system, irrespective of initial P:As ratios. The Eh-pH diagram of the Fe-P-As-H_2O system (Fig. S-4a) also clearly showed the overlapping predominance fields of vivianite and parasymplesite, and is well supported by the calculated mineral stability of the vivianite-parasymplesite solid solution (Fig. S-4b). Following the changes in concentration in the reacting solutions, it is clear that after 1 hr of aging, As and P removal was between 95 to 99 %, while Fe was less efficiently removed (80 to 96 %), revealing that the precipitated solids scavenged the phosphate and arsenate at a similar extent (Table S-3). The similarities and lack of differences between the 1 hr and aged solid phases led us to continue with the solid characterisations only on the 24 hr solids.

The gradual transition from a phosphate to an arsenate structure could be quantified from the XRD patterns, which showed slow structural transition from vivianite to parasymplesite with increasing AsO_4^{3-} mole fraction from 0.22 to 0.95 (Table S-4). These structural changes are evidenced by the displacement of the (100), ($\bar{2}$01), (310) and (201) vivianite reflections (dashed lines in Figs. 1a and S-2). As seen from the vivianite crystal structure model (Fig. S-1), these reflections correspond to lattice planes intersecting the interlinked Fe octahedra *via* PO_4^{3-} or AsO_4^{3-} tetrahedra, which expand at a higher degree of substitution because of the larger thermochemical radius of AsO_4^{3-} (2.48 Å) compared to PO_4^{3-} (2.38 Å) tetrahedra (Frausto da Silva and Williams, 2001). This is also reflected in the larger lattice parameters and associated cell volumes of As-vivianites (Fig. 1b–e) derived from Rietveld refinements (Table S-5, Fig. S-3), which increased linearly and suggest an isomorphous substitution following Vegard's law (Vegard, 1921). Lattice parameters *a*, *b* and *c* increased by 1 to 2 %, while the unit cell volume expanded up to 5 % compared to parasymplesite. The lattice parameters of natural vivianites, rarely occurring parasymplesite (only two refined structures exist in literature), and biogenic As-vivianites are also in agreement with the values obtained in this study (grey coloured symbols in Fig. 1b–e); although variations arising from natural heterogeneity (*e.g.*, partial substitution of Fe(II) sites by divalent cations, structural Fe(II) oxidation) exist in natural mineral specimens.

Morphology of As-vivianites and local distribution of P and As. The synthesised As vivianites (Figs. 2a, S-5a,b) exhibited large platy crystals (between 5–10 μm in length and 2–5 μm in width) elongated along the *a* axis direction and often radiating from the centre, similar to As-free vivianite (Fig. S-5c). In addition, all crystals in the vivianite-parasymplesite solid solution series were extremely thin, ranging from 50 to 100 nm, indicating slow growth of (010).

Mapping the elemental distribution of P and As in As-vivianites (*e.g.*, $x = 0.48$; Fig. 2b–d) by high angular dark field (HAADF) STEM imaging coupled with energy dispersive X-ray (EDX) mapping showed homogeneously distributed P and As in the crystals and no chemical zonation, even at higher magnification (Fig. S-6).

Further increasing the AsO_4^{3-} substitution even to $x = 0.95$, still resulted in plate-like crystals (Fig. S-5b). This is very different to the morphology of synthetic parasymplesite (*i.e.* As end member), which has a needle or lath-type crystal habit (0.5–5 μm in length and 0.5–2 μm in width; Fig. S-5d), indicating preferred crystal growth along the *c* axis. It is worth noting that synthetic As-vivianites had uneven crystal edges compared to synthetic As-free vivianite (Fig. S-5), and that vivianite and all As-vivianites, were extremely beam sensitive, degrading rapidly upon continuous exposure to electrons during imaging (*e.g.*, Fig. S-7).

Local bonding environment and speciation of Fe and As. Distinct features in the Fe K-edge EXAFS spectra clearly showed the gradual transition of Fe local bonding environment (yellow bands in Fig. 3a) with increasing AsO_4^{3-} substitution ($x = 0.22$, 0.48, 0.90). For example, the characteristic, prominent shoulders in the first and second oscillations at 5.2 and 8.0 $Å^{-1}$ in vivianite slowly decreased in intensity as AsO_4^{3-} substitution

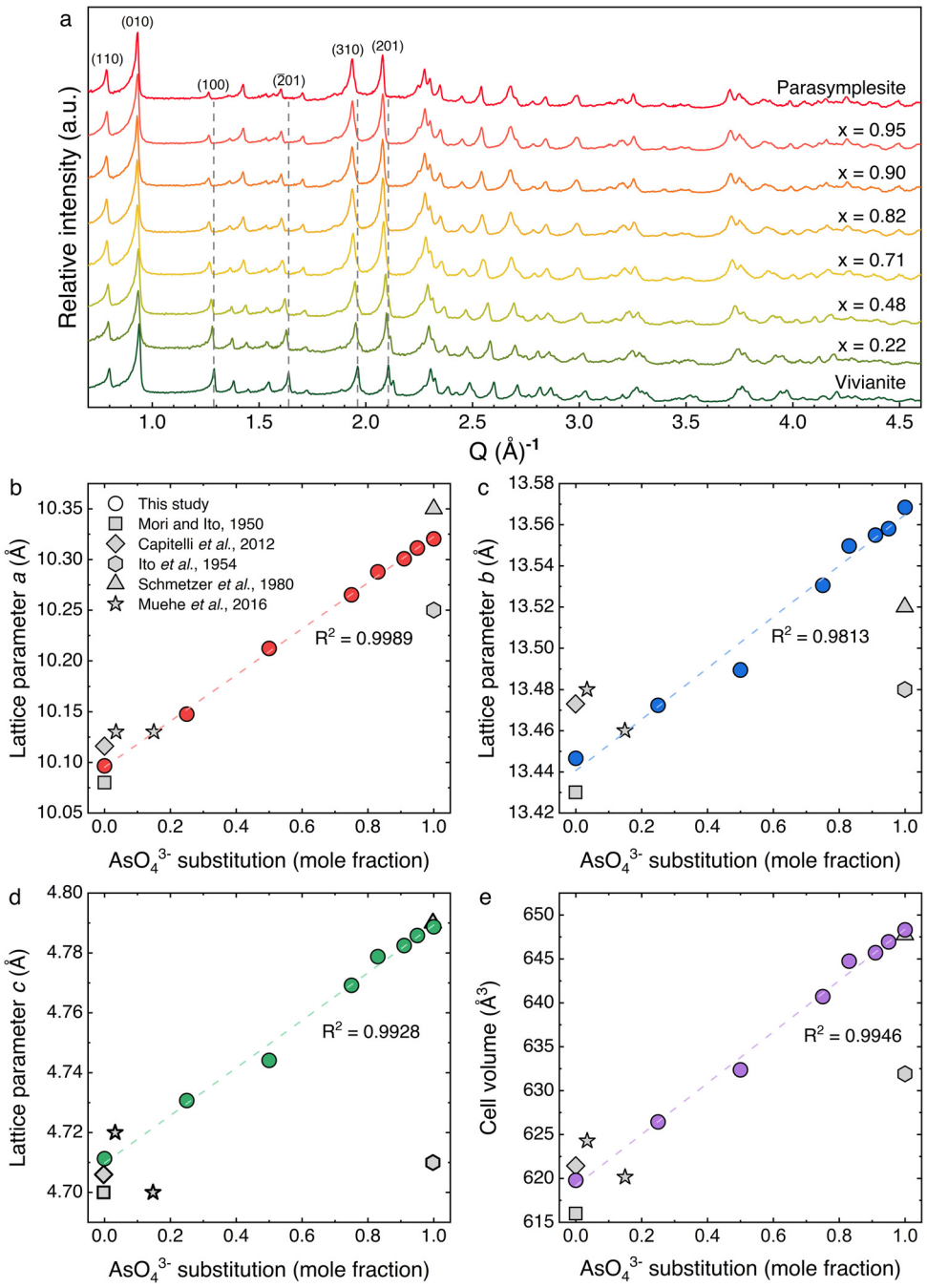

Figure 1 **(a)** XRD patterns of As-substituted vivianites (x = mole fraction of substituted AsO_4^{3-}) aged for 24 hr, plotted in Q-space ($Q = 2\pi/d_{hkl}$). Dashed grey lines indicate displacement in selected lattice planes in vivianite due to AsO_4^{3-} substitution for PO_4^{3-}. Full XRD patterns can be found in Figure S-2. Variations in lattice parameter values **(b–d)** and cell volumes **(e)** of our As-vivianites (coloured circles) compared to literature (Mori and Ito, 1950; Ito *et al.*, 1954; Schmetzer *et al.*, 1980; Capitelli *et al.*, 2012; Muehe *et al.*, 2016) shown as grey symbols. Dashed lines represent linear relationships as a function of As(V) substitution.

increased. Intense oscillations between 8.4 and 10 $Å^{-1}$ also dampened at 48 mol % AsO_4^{3-} substitution, and were replaced by a single oscillation at 90 mol % substitution as the Fe local bonding environment became more parasymplesite-like. The subtle beat feature found in parasymplesite at 7 $Å^{-1}$ only appeared at 90 mol % As(V) substitution (arrows in Fig. 3a). We could not perform shell-by-shell fits on the Fe K-edge EXAFS of As-vivianites because of the lack of spatial resolution required to fit multiple atomic pair paths (*i.e.* Fe-As, Fe-P) in the second shell. However, linear combination fitting (LCF) results of the Fe K-edge EXAFS spectra (Fig. 3b, Table S-6), in combination with our XRD Rietveld refinement, suggest that the Fe local bonding environment gradually changed from a vivianite-like to parasymplesite-like environment as As(V) substitution in the solids increased.

The As K-edge EXAFS spectrum of parasymplesite (topmost spectra; Fig. 3c) has pronounced shoulders in the first and second oscillations at 4.3 and 6.5 $Å^{-1}$, two beat features between 8 and 9 $Å^{-1}$ and a peak splitting in the third oscillation (arrows at $x = 0.90$ in Fig. 3c). These characteristic pronounced shoulders of parasymplesite can be seen in all As-vivianites, irrespective of degree of AsO_4^{3-} substitution. However, the two beat features and peak splitting in the third oscillation (arrows in Fig. 3c) only become apparent at high AsO_4^{3-}

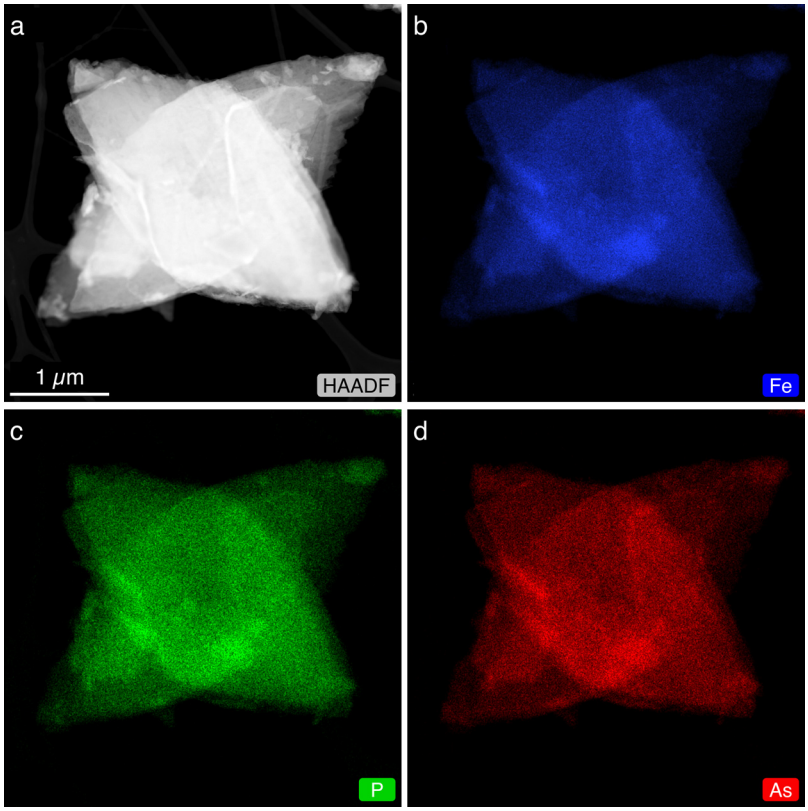

Figure 2 **(a)** HAADF-STEM image of As-substituted vivianite ($x = 0.48$) and corresponding EDX maps: **(b)** Fe (blue); **(c)** P (green); and **(d)** As (red).

substitution ($x \geq 0.90$). Nonetheless, shell-by-shell fitting (Fig. 3d, Table S-7) showed similarities in As local bonding environment in all As-vivianites and parasymplesite, even at low AsO_4^{3-} substitution ($x = 0.22$). In general, the first neighbour contribution to the EXAFS fit correspond to the As-O atomic correlation for tetrahedral AsO_4^{3-} ($R_{As\text{-}O} = 1.69$ Å); the second neighbour contribution arises from As-Fe atomic pairs of two corner-sharing linkages between AsO_4^{3-} tetrahedron and two Fe octahedra ($R_{As\text{-}Fe1} \approx 3.30$ Å, $R_{As\text{-}Fe2} \approx 3.47$ Å; Fig. S-8). These fit-derived interatomic distances are in excellent agreement with crystallographic values for parasymplesite (Mori and Ito, 1950), and are consistent with EXAFS-derived Fe-As distances in parasymplesite (Jönsson and Sherman, 2008).

More importantly, As(V) was not reduced by aqueous or structural Fe(II) during As-vivianite crystallisation. This is evident from the positions of the Fe and As K-edge X-ray absorption near edge structure (XANES) maxima of As-vivianites ($x = 0.22$, 0.48, 0.90) centred at 7,127 and 11,874 eV, respectively (Fig. S-9). These positions match the reference vivianite and parasymplesite, as well as other vivianites reported in literature (Miot *et al.*, 2009; Muehe *et al.*, 2016).

Our As K-edge EXAFS results are also supported by the FTIR data (Figs. 4, S-10), which confirmed increased AsO_4^{3-} substitution through gradually increasing intensities of $\nu(AsO_4)$ bands between ~885 and 700 cm^{-1} at the expense of $\nu(PO_4)$ bands between ~1120 and 885 cm^{-1} (Table S-8). The shoulder at ~792 cm^{-1} [$\nu(AsO_4)$] only appeared in the spectra of As-vivianite with >71 mol % substitution. At even higher AsO_4^{3-} substitution, a new band appeared at ~1076 cm^{-1} and the 1035 cm^{-1} band split into two component bands at 1042 and 1022 cm^{-1}, representing $\nu(PO_4)$ antisymmetric stretching modes (Makreski *et al.*, 2015). Substitution of AsO_4^{3-} in vivianite also affects the bonding environment of structural water; however, interpretation of the ν(OH) and δ(HOH) regions can be complicated (see further discussion in Supplementary Information S-2.5).

Naturally, the question arises whether As(V) is adsorbed to vivianite surfaces (*cf.* Thinnappan *et al.*, 2008), as in the case of other Fe(II)-bearing minerals. The As-Fe atomic distance for As(V) adsorbed as bidentate binuclear (^2C) and monodentate mononuclear (^1V) inner sphere surface complexes are $R_{As\text{-}Fe}$ of ~3.4 and ~3.5 Å, respectively (Jönsson and Sherman, 2008; Perez *et al.*, 2020), similar to our fit-derived distances for As-vivianites. We attempted to fit these two As-Fe paths to the second neighbour contribution of As-vivianites individually, but the fit yielded unrealistic CN values (*i.e.* negative, or extremely high CN values). To distinguish potentially adsorbed As(V) species in our As-vivianites, we reacted As(V) ($[As]_{initial} = 4$ mM) with pure vivianite ($[Fe]_{vivianite} = 12$ mM) at pH ~ 7 for 24 hr, comparable to the 48 mol % substituted As-vivianite. Structurally incorporated As would have resulted in shifts in vivianite reflections (*cf.* Fig. 1), but the XRD pattern of As-adsorbed vivianite was equivalent to the pure vivianite (Fig. S-11a). In addition, the $\nu(AsO_4)$ band in the FTIR spectrum (Fig. S-11b) of As-adsorbed vivianite only exhibited a very weak shoulder feature at ~780 cm^{-1} instead of the characteristic sharp bands seen in As-vivianites and parasymplesite (*cf.* Fig. 4). More importantly, adsorbed As(V) would not systematically decrease the intensities of $\nu(PO_4)$ bands in As-vivianites. SEM-EDX maps of As-adsorbed vivianite (Fig. S-12) also showed clear differences in As signal intensities and distribution compared to 48 mol % substituted As-vivianite (Fig. S-13). Overall, these results can be interpreted as arsenic being primarily structurally incorporated in As-vivianites, with only minor contributions from adsorbed species, if at all present.

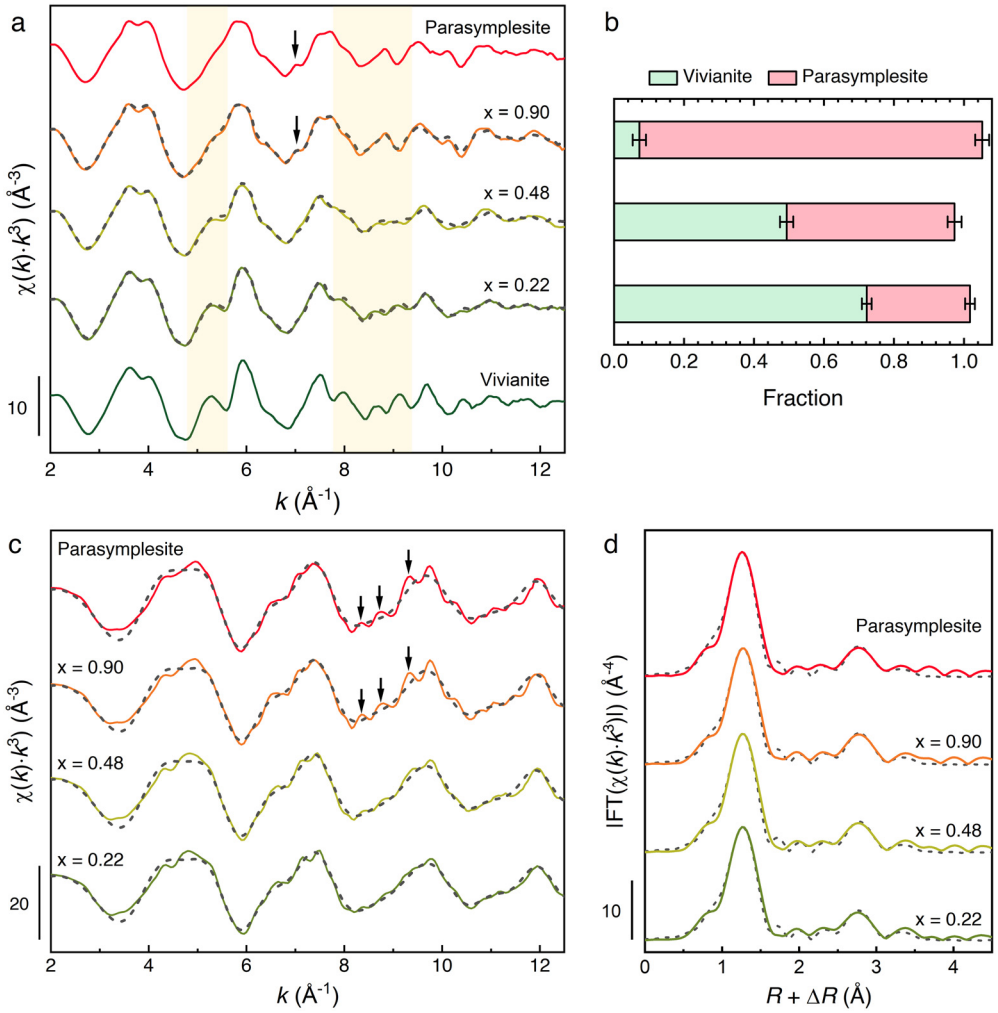

Figure 3 **(a)** Fe K-edge k^3-weighted EXAFS spectra of As-vivianites. Dashed grey lines denote **(b)** LCF of Fe K-edge EXAFS spectra of mineral end members (*i.e.* vivianite, parasymplesite). **(c)** As K-edge k^3-weighted EXAFS spectra of As vivianites and **(d)** corresponding Fourier transform magnitude. Dashed grey lines denote shell-by-shell fits.

Geochemical Implications

In this study, we explored the structural incorporation of As(V) in vivianite under anoxic conditions. Our complementary results (Fig. S-14) document and cross correlate that AsO_4^{3-} can systematically substitute for PO_4^{3-} in the vivianite crystal structure, thereby forming a continuous solid solution. We have showed that up to 95 mol % (~24 wt. %) of As(V) can be incorporated (Table S-4), with a very minor fraction of potentially adsorbed species. Sequestration of As(V) in vivianite *via* partial substitution for PO_4^{3-} under reduced conditions is favourable because most Fe(II)-bearing minerals have far lower As uptake, and sorption mechanisms are more susceptible to remobilisation upon desorption. Compared to interactions with other common Fe(II)-bearing minerals in ferruginous environments, where arsenic is primarily adsorbed and only reaches ~15 wt. % in magnetite (Yean *et al.*, 2005) or ~9 wt. % in green rust (Perez *et al.*, 2019), our current results show that arsenic incorporation into vivianite could be stable sinks for As(V) removal in ferruginous settings. For example, vivianite found in anoxic, non-sulfidic environments could incorporate major and trace elements (Vuillemin *et al.*, 2020; Kubeneck *et al.*, 2023). Therefore, As-vivianites may be present, yet so far undocumented in contaminated, anoxic settings such as in Bangladesh where vivianite and parasymplesite are both saturated (Johnston and Singer, 2007). However, since naturally occurring As-vivianites have yet to be found, their stability as a sink for arsenic under environmentally relevant conditions needs to be evaluated in further studies. In addition to the potential importance of As-vivianites in contaminated settings, our findings have implications for phosphorus

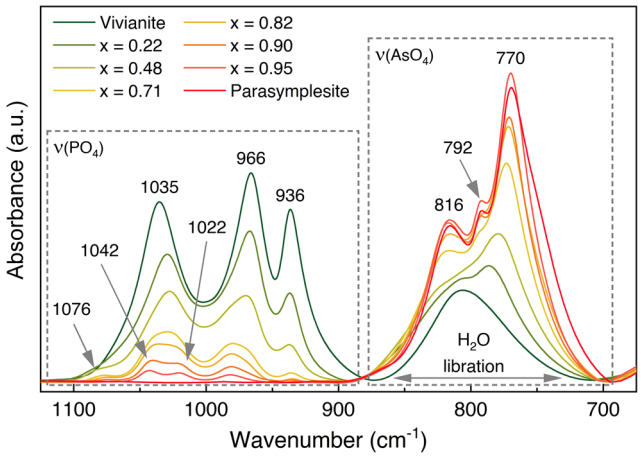

Figure 4 FTIR spectra of As(V)-substituted vivianites showing stretching regions for phosphate [$\nu(PO_4)$] and arsenate [$\nu(AsO_4)$], and H_2O libration vibrations. Full spectra and band assignments can be found in Figures S-10 and Table S-8, respectively.

(and arsenic) cycling since vivianite has been suggested as a P sink in Precambrian oceans (Hao *et al.*, 2020), and modern lake analogues (Xiong *et al.*, 2019; Vuillemin *et al.*, 2020). Given the widespread occurrence of arsenate in these ancient oceans (Chi Fru *et al.*, 2016), As(V) substitution for P in vivianites would have reduced the bioavailability of toxic As species, and could have shaped how life emerged and adapted in the Precambrian oceans (Visscher *et al.*, 2020).

Acknowledgements

This project has received funding from the European Union's Horizon 2020 Marie Skłodowska-Curie Innovative Training Network METAL-AID (grant no. 675219), Helmholtz Recruiting Initiative awarded to LGB (award no. I-044-16-01), GFZ expedition fund (grant no. X-044-20-01) for support for travel to the synchrotron facility, and Deutsche Forschungsgemeinschaft (DFG, German Research Foundation) "Open Access Publikationskosten" funding programme (project no. 491075472). JPHP acknowledges the Royal Society of Chemistry (RSC) for the Researcher Development Grant (grant no. D22-2132977309). MO was funded by the Förderverein Chemie-Olympiade (FChO) during her research internship. ICP-OES analyses were carried out at the Helmholtz Laboratory for the Geochemistry of the Earth Surface (HELGES) at GFZ Potsdam. The authors especially thank the European Development Fund and the state of Brandenburg for the Themis Z S/TEM, a part of the Potsdam Imaging and Spectral Analysis (PISA) Facility at GFZ Potsdam. SEM-EDX maps of the As-adsorbed vivianite were collected with the help of Marcin Daniel Syczewski. We acknowledge Diamond Light Source for time on I20-scanning beamline under proposal SP23496-1, with thanks to Shu Hayama for assistance. We also like to thank Dominique J. Tobler and Thaïs Couasnon for their help during beamtime.

Editor: Juan Liu

Additional Information

Supplementary Information accompanies this letter at https://www.geochemicalperspectivesletters.org/article2325.

Cite this letter as: Perez, J.P.H., Okhrymenko, M., Blukis, R., Roddatis, V., Mayanna, S., Mosselmans, J.F.W., Benning, L.G. (2023) Vivianite-parasymplesite solid solution: A sink for arsenic in ferruginous environments? *Geochem. Persp. Let.* 26, 50–56. https://doi.org/10.7185/geochemlet.2325

References

Al-Borno, A., Tomson, M.B. (1994) The temperature dependence of the solubility product constant of vivianite. *Geochimica et Cosmochimica Acta* 58, 5373–5378. https://doi.org/10.1016/0016-7037(94)90236-4

Anthony, J.W., Bideaux, R.A., Bladh, K.W., Nichols, M.C. (2000) *Handbook of Mineralogy Volume IV: Arsenates, Phosphates and Vanadates*. Mineral Data Publishing, Tucson, Arizona, USA.

Bartl, H. (1989) Water of crystallization and its hydrogen-bonded crosslinking in vivianite $Fe_3(PO_4)_2 \cdot 8H_2O$; a neutron diffraction investigation. *Fresenius' Zeitschrift für analytische Chemie* 333, 401–403. https://doi.org/10.1007/BF00572335

Capitelli, F., Chita, G., Ghiara, M.R., Rossi, M. (2012) Crystal-chemical investigation of $Fe_3(PO_4)_2 \cdot 8\,H_2O$ vivianite minerals. *Zeitschrift für Kristallographie - Crystalline Materials* 227, 92–101. https://doi.org/10.1524/zkri.2012.1442

Chi Fru, E., Arvestål, E., Callac, N., El Albani, A., Kilias, S., Argyraki, A., Jakobsson, M. (2016) Arsenic stress after the Proterozoic glaciations. *Scientific Reports* 5, 17789. https://doi.org/10.1038/srep17789

Egger, M., Jilbert, T., Behrends, T., Rivard, C., Slomp, C.P. (2015) Vivianite is a major sink for phosphorus in methanogenic coastal surface sediments. *Geochimica et Cosmochimica Acta* 169, 217–235. https://doi.org/10.1016/j.gca.2015.09.012

Filippelli, G.M. (2002) The Global Phosphorus Cycle. In: Kohn, M.J., Rakovan, J., Hughes, J.M. (Eds.) *Phosphates: Geochemical, Geobiological, and Materials Importance*. Reviews in Mineralogy and Geochemistry 48, 391–425. https://doi.org/10.2138/rmg.2002.48.10

Frausto da Silva, J.J.R., Williams, R.J.P. (2001) *The Biological Chemistry of the Elements: The Inorganic Chemistry of Life*. Oxford University Press, Oxford.

Hao, J., Knoll, A.H., Huang, F., Schieber, J., Hazen, R.M., Daniel, I. (2020) Cycling phosphorus on the Archean Earth: Part II. Phosphorus limitation on primary production in Archean ecosystems. *Geochimica et Cosmochimica Acta* 280, 360–377. https://doi.org/10.1016/j.gca.2020.04.005

Heiberg, L., Koch, C.B., Kjaergaard, C., Jensen, H.S., Hansen, H.C.B. (2012) Vivianite Precipitation and Phosphate Sorption following Iron Reduction in Anoxic Soils. *Journal of Environmental Quality* 41, 938–949. https://doi.org/10.2134/jeq2011.0067

Ito, T.-i., Minato, H., Sakurai, K.'i. (1954) Parasymplesite, a New Mineral Potymorphous with Symplesite. *Proceedings of the Japan Academy* 30, 318–324. https://doi.org/10.2183/pjab1945.30.318

Johnston, R.B., Singer, P.C. (2007) Solubility of Symplesite (Ferrous Arsenate): Implications for Reduced Groundwaters and Other Geochemical Environments. *Soil Science Society of America Journal* 71, 101–107. https://doi.org/10.2136/sssaj2006.0023

Jönsson, J., Sherman, D.M. (2008) Sorption of As(III) and As(V) to siderite, green rust (fougerite) and magnetite: Implications for arsenic release in anoxic groundwaters. *Chemical Geology* 255, 173–181. https://doi.org/10.1016/j.chemgeo.2008.06.036

Kubeneck, L.J., ThomasArrigo, L.K., Rothwell, K.A., Kaegi, R., Kretzschmar, R. (2023) Competitive incorporation of Mn and Mg in vivianite at varying salinity and effects on crystal structure and morphology. *Geochimica et Cosmochimica Acta* 346, 231–244. https://doi.org/10.1016/j.gca.2023.01.029

Makreski, P., Stefov, S., Pejov, L., Jovanovski, G. (2015) Theoretical and experimental study of the vibrational spectra of (para)symplesite and hornesite. *Spectrochimica Acta Part A: Molecular and Biomolecular Spectroscopy* 144, 155–162. https://doi.org/10.1016/j.saa.2015.01.108

Miot, J., Benzerara, K., Morin, G., Bernard, S., Beyssac, O., Larquet, E., Kappler, A., Guyot, F. (2009) Transformation of vivianite by anaerobic nitrate-reducing iron-oxidizing bacteria. *Geobiology* 7, 373–384. https://doi.org/10.1111/j.1472-4669.2009.00203.x

Mori, H., Ito, T. (1950) The Structure of Vivianite and Symplesite. *Acta Crystallographica* 3, 1–6. https://doi.org/10.1107/S0365110X5000001X

Muehe, E.M., Morin, G., Scheer, L., Le Pape, P., Esteve, I., Daus, B., Kappler, A. (2016) Arsenic(V) Incorporation in Vivianite during Microbial Reduction of Arsenic (V)-Bearing Biogenic Fe(III) (Oxyhydr)oxides. *Environmental Science & Technology* 50, 2281–2291. https://doi.org/10.1021/acs.est.5b04625

Nriagu, J.O. (1972) Stability of vivianite and ion-pair formation in the system $Fe_3(PO_4)_2$-H_3PO_4-H_2O. *Geochimica et Cosmochimica Acta* 36, 459–470. https://doi.org/10.1016/0016-7037(72)90035-X

Patrick Jr., W.H., Khalid, R.A. (1974) Phosphate Release and Sorption by Soils and Sediments: Effect of Aerobic and Anaerobic Conditions. *Science* 186, 53–55. https://doi.org/10.1126/science.186.4158.53

Perez, J.P.H., Freeman, H.M., Schuessler, J.A., Benning, L.G. (2019) The interfacial reactivity of arsenic species with green rust sulfate (GR_{SO4}). *Science of The Total Environment* 648, 1161–1170. https://doi.org/10.1016/j.scitotenv.2018.08.163

Perez, J.P.H., Freeman, H.M., Brown, A.P., van Genuchten, C.M., Dideriksen, K., S'Ari, M., Tobler, D.J., Benning, L.G. (2020) Direct Visualization of Arsenic Binding on Green Rust Sulfate. *Environmental Science & Technology* 54, 3297–3305. https://doi.org/10.1021/acs.est.9b07092

Schmetzer, K., Tremmel, G., Bartelke, W. (1980) Eine Paragenese seltener Minerale aus Bou-Azzer, Marokko: Parasymplesit, Symplesit, Schneiderhöhnit, Karibibit. *Neues Jahrbuch für Mineralogie - Abhandlungen* 138, 94–108.

Thinnappan, V., Merrifield, C.M., Islam, F.S., Polya, D.A., Wincott, P., Wogelius, R.A. (2008) A combined experimental study of vivianite and

As (V) reactivity in the pH range 2–11. *Applied Geochemistry* 23, 3187–3204. https://doi.org/10.1016/j.apgeochem.2008.07.001

Vegard, L. (1921) Die Konstitution der Mischkristalle und die Raumfüllung der Atome. *Zeitschrift für Physik* 5, 17–26. https://doi.org/10.1007/BF01349680

Visscher, P.T., Gallagher, K.L., Bouton, A., Farias, M.E., Kurth, D., Sancho-Tomás, M., Philippot, P., Somogyi, A., Medjoubi, K., Vennin, E., Bourillot, R., Walter, M.R., Burns, B.P., Contreras, M., Dupraz, C. (2020) Modern arsenotrophic microbial mats provide an analogue for life in the anoxic Archean. *Communications Earth & Environment* 1, 24. https://doi.org/10.1038/s43247-020-00025-2

Vuillemin, A., Friese, A., Wirth, R., Schuessler, J.A., Schleicher, A.M., Kemnitz, H., Lücke, A., Bauer, K.W., Nomosatryo, S., von Blanckenburg, F., Simister, R., Ordoñez, L.G., Ariztegui, D., Henny, C., Russell, J.M., Bijaksana, S., Vogel, H., Crowe, S.A., Kallmeyer, J., the Towuti Drilling Project Science team (2020) Vivianite formation in ferruginous sediments from Lake Towuti, Indonesia. *Biogeosciences* 17, 1955–1973. https://doi.org/10.5194/bg-17-1955-2020

Walpersdorf, E., Bender Koch, C., Heiberg, L., O'Connell, D.W., Kjaergaard, C., Bruun Hansen, H.C. (2013) Does vivianite control phosphate solubility in anoxic meadow soils? *Geoderma* 193–194, 189–199. https://doi.org/10.1016/j.geoderma.2012.10.003

Xiong, Y., Guilbaud, R., Peacock, C.L., Cox, R.P., Canfield, D.E., Krom, M.D., Poulton, S.W. (2019) Phosphorus cycling in Lake Cadagno, Switzerland: A low sulfate euxinic ocean analogue. *Geochimica et Cosmochimica Acta* 251, 116–135. https://doi.org/10.1016/j.gca.2019.02.011

Yean, S., Cong, L., Yavuz, C.T., Mayo, J.T., Yu, W.W., Kan, A.T., Colvin, V.L., Tomson, M.B. (2005) Effect of magnetite particle size on adsorption and desorption of arsenite and arsenate. *Journal of Materials Research* 20, 3255–3264. https://doi.org/10.1557/jmr.2005.0403

Geochemical Perspectives Letters

Vivianite-parasymplesite solid solution: A sink for arsenic in ferruginous environments?

J.P.H. Perez, M. Okhrymenko, R. Blukis, V. Roddatis, S. Mayanna, J.F.W. Mosselmans, L.G. Benning

Supplementary Information

The Supplementary Information includes:

- S-1 Elemental Concentration Analysis
- S-2 Material Characterization
- Supplementary Tables S-1 to S-8
- Supplementary Figures S-1 to S-16
- Supplementary Information References

S-1 Elemental Concentration Analysis

After the precipitation of the As-substituted vivianites, an aliquot of the suspension was sampled and added to a 0.3 M HNO_3 solution for the analysis of the total elemental concentration. The liquid phase was obtained by filtering the suspension though a 0.2-µm polycarbonate membrane filter, and then acidified using concentrated HNO_3 (Aristar® for trace analysis). Acidified samples were stored at ~4 °C until analysis. The elemental composition of precipitates was calculated from the difference between the concentrations in the suspension and liquid phase, determined from inductively coupled plasma optical emission spectrometry (ICP-OES, Varian 720ES) as described in our previous study (Perez *et al.*, 2019).

Acidified liquid samples (pH ≈ 2) were diluted gravimetrically in acid-cleaned polypropylene (PP) tubes prior to inductively coupled plasma optical emission spectrometry (ICP-OES) analyses. Sample dilutions were performed using 0.3 M HNO_3 (Merck Suprapur® grade) containing 1 mg g^{-1} Cs as an ionisation buffer to achieve matrix matching with calibration standards prepared from a mixture of single ICP element standards (Merck Certipur®, traceable to NIST reference materials). Scandium (1 µg g^{-1}) was added as an internal standard. Dilution factors were adapted to ensure that analyte solutions were within the concentration range of the matrix-matched calibration standards (linearity criteria $R^2 > 0.9990$) and with final HNO_3 and Cs concentrations of 0.3 M and 1 mg g^{-1}, respectively.

For each analytical session, instrumental stability and drift were monitored using Ar, Cs and Sc at emission wavelengths of 420.067, 459.311 and 335.372 nm for each sample analysis, respectively, as well as regular measurements of a quality control (QC) solution, similar to sample compositions. Instrumental statistical limits of detection (LoD = 3 s.d. above background) or limits of quantification (LoQ = 10 s.d. above background) were determined in each analytical session based on nine repeat analysis of 0.3 M HNO_3 (+1 mg g^{-1} Cs) used for sample dilution.

Concentrations of As, P and Fe in the samples were evaluated using the emission wavelengths of 193.696, 214.914 and 261.382 nm, respectively. The determined LoD values were 0.011 µg g^{-1} for As, 0.022 µg g^{-1} for P and 0.012 µg g^{-1} for Fe. Analytical uncertainties at a 95 % confidence level for concentrations quantified (above LoQ) during this study are ~5 % relative, verified by repeat analyses of a QC solution, which was similar to the sample compositions (Table S-1).

S-2 Material Characterisation

S-2.1 Powder X-ray diffraction (XRD) and Rietveld refinement

Samples for XRD measurements were loaded into glass capillaries (ø = 0.5 mm, Hilgenberg glass capillary no. 50) and sealed with Cristaseal wax (Hawksley & Sons Ltd.) inside the anaerobic chamber. XRD patterns were recorded using a STOE STADI P X-ray diffractometer operated in Debye-Scherrer geometry using Ag $K\alpha_1$ radiation (λ = 0.56087 Å) from a primary beam Ge(111) monochromator and equipped with two DECTRIS MYTHEN2 R 1K position sensitive detectors. Scattered X-rays were collected over the *Q*-range of 0 to ~13.4 $Å^{-1}$. Each sample measurement lasted for 2.5 h, and samples were spun during data collection for improved particle statistics. Rietveld analysis of the XRD patterns was performed using the GSAS-II software (Toby and Von Dreele, 2013). Instrument function parameters were obtained by fitting NIST LaB_6 standard diffraction peaks. The samples were modelled as a single phase vivianite or parasymplesite (*C2*/*m* symmetry) (Mori and Ito, 1950), and considered as a perfect solid solution with P/As site being occupied by either P or As. The background was approximated with ten Chebyschev polynomials. Refined parameters included unit cell, grain size, microstrain, As/P ratio, thermal displacement and atomic position parameters. Grain size was modelled using uniaxial approximation with (001) being the unique axis in accordance with observations with SEM/TEM.

S-2.2 Scanning electron microscopy (SEM)

Samples for SEM were prepared inside an anaerobic chamber by fixing the dried powder samples onto a double-sided carbon tape attached to SEM stubs. Stubs were put inside an anaerobic jar to minimize oxidation during rapid transfer to the SEM, quickly loaded into vacuum sputter coater (BAL-TEC MED 020 Leica Microsystems) and coated (*ca*. 5–8 nm thick) with carbon to avoid charging effects during imaging. SEM images were acquired using a ZEISS Ultra Plus FEG-SEM operated in high vacuum mode at an acceleration voltage of 3 kV with 10 µm aperture size using an InLens secondary electron detector. Elemental analyses of samples were performed at 20 kV with 120 µm aperture size in point and shoot mode using a Thermo Scientific Ultra Dry Energy Dispersive Spectrometry (EDX) detector.

S-2.3 Transmission electron microscopy (TEM)

Dry powder samples were loaded in screw capped sample vials inside the anaerobic chamber and then transported to the sample preparation lab. Samples were ground in ethanol using an agate mortar and pestle, and immediately drop-casted onto a holey amorphous coated carbon copper grid. HAADF-STEM images and EDX maps were recorded using a Thermo Fisher Scientific™ Themis Z (3.1) Scanning Transmission Electron Microscope operated at 300 kV and equipped with a Super-X EDX system, and a Gatan Continuum ER/1065 imaging filter.

S-2.4 X-ray absorption spectroscopy

The pellets were prepared inside the anaerobic chamber at GFZ Potsdam by mixing dry powder samples with cellulose using an agate mortar and pestle. Mixture calculations were performed using XAFSmass software (Klementiev and Chernikov, 2016). Pellets were sealed inside sample holders made of two layers of single-sided 70-µm thick Kapton® polyimide tape. The Kapton-sealed pellet samples were placed inside air-tight headspace crimp vials stored inside an anaerobic jar to prevent oxidation during sample transport to the beamline. The sample vials were immediately

transferred to the glovebox (Ar atmosphere, MBRAUN) upon arrival at the beamline. The Kapton-sealed samples were fixed onto a sample holder provided by the beamline and then transferred to the station using an anaerobic jar.

Fe and As K-edge XAS data were collected at I20-scanning of Diamond Light Source (UK) (Diaz-Moreno *et al.*, 2018). Spectra were recorded at liquid nitrogen (LN_2) temperatures (~77 K) both in transmission and fluorescence mode to a reciprocal space value of ~14.8 $Å^{-1}$. For this, a LN_2 cryostat with a helium convection (Optistat DN2, Oxford Instruments). Fluorescence data was collected using a 64-element Ge solid-state detector equipped with Xspress4. The vertical dimension of the X-ray beam during data collection was 400 µm and the horizontal dimension was 300 µm. To prevent second-order harmonics, rejection mirrors were used. A Si(111) crystal pair ($\Delta E/E = 1.3 \times 10^{-4}$) with a fixed beam exit was used as a monochromator. The maximum in the first derivative of X-ray absorption spectra from Fe and Au foils were used to calibrate the beam at 7112 eV (Fe K-edge) and 11,919 eV (Au L_3 edge), respectively. The XANES region was measured with 0.3 eV steps. Three to four scans were collected for each sample depending on data quality. During the data collection, changes in line shape and peak position indicative of beam-induced redox reactions were examined and, however, no beam damage was observed.

Spectra were aligned, averaged, and background-subtracted using the SIXpack software (Webb, 2005). Shell-by-shell fits of the As K-edge EXAFS spectra were performed from 1 to 4 Å in $R + \Delta R$-space using SIXpack software, based on algorithms derived from IFEFFIT (Newville, 2001). The fits typically included the interatomic distance (R), the coordination number (CN), the mean squared atomic displacement parameter (σ^2), and the change in threshold energy (ΔE_0) for one sample. Phase and amplitude functions for single and multiple scattering paths were calculated using FEFF6 (Rehr *et al.*, 1992) and As atomic pair paths (*i.e.* As-O, As-O-O and As-Fe/Fe-As) were derived from the crystal structure of paths from scorodite (Kitahama *et al.*, 1975). In the preliminary shell-by-shell fits, CN and σ^2 were found to be highly correlated, producing high fit-derived standard errors in these fitting parameters. The σ^2 values of the As-Fe path was therefore constrained to 0.004 (Muehe *et al.*, 2016) to reduce the high degree of correlations. Consistent with previous works (Paktunc *et al.*, 2008; Mikutta *et al.*, 2010), the passive electron reduction parameter (S_0^2) in each fit was set to 1.0. The goodness-of-fit was assessed based on the R-factor, which is defined as the mean square difference between the fit and the data on a point-by-point basis: R-factor = $\sum_i (\text{data}_i - \text{fit}_i)^2 / \sum_i (\text{data}_i)^2$. An R-factor of <0.05 is considered to reflect a reasonable fit (Kelly *et al.*, 2008).

S-2.5 Infrared spectroscopy and spectra interpretation

Dry powder samples were placed inside 2-mL glass vial and then put in crimp capped glass vials to prevent oxidation during transport. Sample vials were opened just before each spectrum was collected. Spectra were acquired using a Nicolet iS5 Fourier Transform infrared spectrometer (Thermo Fisher Scientific™) equipped with a diamond attenuated total reflection (ATR) accessory (iD7 ATR, Thermo Fisher Scientific™). Spectra were collected over the 4000–400 cm^{-1} range with a resolution of 4 cm^{-1} by averaging 64 individual scans. Baseline correction and peak fitting were done using the OMNIC software (Thermo Fisher Scientific™). For integrated area calculations, bands between ~1200 to ~600 cm^{-1} (*i.e.* PO_4^{3-} and AsO_4^{3-} stretching regions) were fitted using a Gauss-Lorentzian function (Gauss amount ≥ 0.7) and the minimum number of component bands possible.

Interpretation of the phosphate [v(PO₄)] and arsenate [v(AsO₄)] stretching regions. As-free vivianite is characterized by three distinct bands at 1035, 966 and 936 cm^{-1}, assigned antisymmetric (ν_3) and symmetric (ν_1) P-O stretching vibrations (Frost *et al.*, 2002). Parasymplesite, on the other hand, is characterized by a sharp band at 770 cm^{-1} with a prominent shoulder at 792 cm^{-1} both arising from As-O antisymmetric stretching vibrations (ν_3) (Frost *et al.*, 2003). The strong band at 806 cm^{-1} in vivianite and 816 cm^{-1} in parasymplesite are attributed to the water librational mode, arising from lattice water molecules.

Interpretation of the water hydroxyl stretching v(OH) and water HOH bending δ(HOH) regions. There are two distinct types of lattice water molecules (O_w1 and O_w2) in the crystal structure of vivianite arsenates that form an intricate network of hydrogen bonds (see Fig. S-1). Type-1 H_2O molecules refer to those found in the Fe1 site (O_W1), which form strong H-bonds by donating their protons to oxygen atoms of adjacent PO_4^{3-} or AsO_4^{3-} tetrahedra in the same layer (Capitelli *et al.*, 2012). Meanwhile, type-2 H_2O molecules in the Fe2 site (O_W2) form strong H-bonds with oxygen atoms of adjacent PO_4^{3-} or AsO_4^{3-} tetrahedra, as well as weaker H-bonds by donating their proton towards other

H_2O molecules in the next layer (*i.e.* lateral connection) (Bartl, 1989). The strength of these H-bonds is reflected in the ν(OH) region. Weakly H-bonded H_2O molecules (shorter H-bond length) in As(V)-substituted vivianites can be attributed to the narrow band at ~3400 cm^{-1} in the IR spectra, while the broad band at ~3100 cm^{-1} corresponds to strongly H-bonded water molecules (longer H-bond length; inset, Fig. S-10) (Frost *et al.*, 2002, 2003). It must be noted, however, that the interpretation of the ν(OH) and δ(HOH) regions can be complicated, as seen from our IR analysis of (partially) deuterated vivianite.

In partially deuterated vivianite, ν(OH) modes between 2700 and 3500 cm^{-1} partially move to between 2100 and 2600 cm^{-1}; however, the shape of the deuterated peaks is very different (Fig. S-15). In deuterated vivianite, the peaks can be fitted with only four Voigt functions (two symmetric and two antisymmetric ν(OH) modes; Fig. S-16a). Voigt 4 is very broad and therefore most likely contain contribution from adsorbed water that was not removed by drying properly. The shapes of the peaks may not be perfectly describable with Voigt functions; however, this is not an uncommon feature in ν(OH) bands of minerals (Ratajczak and Yaremko, 2000). The very different shape of ν(OH) bands of protic vivianite indicate additional contributions to the absorption of peaks of protic water by additional components. The most likely additions are combination bands that have enhanced intensity due to Fermi resonance as has been observed in previous studies of hydrated phosphates (Šoptrajanov *et al.*, 2002). Such Fermi resonance enhanced bands make interpretation and peak assignment in the ν(OH) region very complicated.

Vivianite contains two distinct water molecules; therefore, vivianite IR spectrum should have only two peaks in the δ(HOH) region near 1600 cm^{-1}. However, as observed in this work as well as others (Frost *et al.*, 2002, 2003), the δ(HOH) region can only be described with at least 3 distinct peaks. However, in the deuterated vivianite (Fig. S-16b), only two peaks are needed, indicating this extra peak does not originate from some δ(HOH). It can be observed that there is a very strong water libration mode at about half the frequency of the δ(HOH) modes. Water libration mode has a very broad peak, like the one observed in the bending region. Therefore, this additional peak is most likely an overtone of water libration mode. As libration involves the movement of the entire molecule, the effect of deuteration has little effect on its frequency (change of 18 *vs*. 19 or 20 g mol^{-1}, 5 to 10 % change). By applying Morse oscillator model, water libration mode can be described as having fundamental frequency $\omega_0 = 845$ cm^{-1} and anharmonicity parameter $\chi = 0.024$. There can even be seen a potential very small hint of a broad peak at 2287 cm^{-1} which would correspond to the second overtone of the same vibration mode, and would be consistent with predictions form the Morse model.

S-2.6 Geochemical modelling

Geochemical calculations were carried out in The Geochemist's Workbench® (GWB) 2023 (Bethke, 2010) using the MINTEQ database. Since the solubility constant (K_{sp}) of parasymplesite ($pK_{sp} = 33.25$) were missing, the data reported by Johnston and Singer (2007) were added in the MINTEQ database. We also modified the pK_{sp} of vivianite to 35.8 based on the solubility data from (Al-Borno and Tomson, 1994) in the database. Thermodynamically stable iron (oxyhydr)oxides (*e.g.*, hematite, magnetite, goethite, lepidocrocite) were suppressed successively for calculations involving thermodynamically metastable Fe phases. The reaction of HS^- and SO_4^{2-} was also decoupled to model ferruginous (*i.e.* anoxic, non-sulfidic) conditions.

S-2.7 Calculation of the degree of substitution in the As-vivianite samples

The extent of As incorporation in As-vivianites (mole fraction of AsO_4^{3-} substituted, x_{AsO4}) was estimated using different characterization methods.

ICP-OES analysis. The x_{AsO4} of the As-vivianites was determined using the formula:

$$x_{AsO_4} = \frac{[AsO_4^{3-}]_{solid}}{[AsO_4^{3-}]_{solid} + [PO_4^{3-}]_{solid}} \quad \text{(eq. S-1)}$$

$$x_{AsO_4} = \frac{([AsO_4^{3-}]_{susp} - [AsO_4^{3-}]_{snt})}{([AsO_4^{3-}]_{susp} - [AsO_4^{3-}]_{snt}) + ([PO_4^{3-}]_{susp} - [PO_4^{3-}]_{snt})} \quad \text{(eq. S-2)}$$

where: $[YO_4^{3-}]_{solid}$ concentration of AsO_4^{3-} or PO_4^{3-} in the solids (*Y* representing As or P), calculated from the difference in their concentration in the acidified suspension and supernatant (see Text S-1);
$[YO_4^{3-}]_{susp}$ concentration of AsO_4^{3-} or PO_4^{3-} in the acidified mineral suspension;
$[YO_4^{3-}]_{snt}$ concentration of AsO_4^{3-} or PO_4^{3-} in the acidified supernatant.

Rietveld refinement of XRD data. The x_{AsO4} of the As-vivianites was obtained from the Rietveld refinement of the XRD patterns (see Text S-2.1). In brief, two atoms (*i.e.* As and P) were included in the crystal structure, and were set as equivalent during refinement, forcing both atoms to have the same *x*, *y*, *z* positions and thermal displacement. The site occupancy was refined by constraining the sum of the fraction of As and P to 1 (*i.e.* $f_{As} + f_P = 1$). Only one phase was used during the refinement to reflect a true solid solution, and not just a mixture of the end-members vivianite and parasymplesite. Refinements showed that a two end-member phase model was found to be inconsistent with the XRD data.

SEM-EDX analysis. The x_{AsO4} of As-vivianites was estimated (semi-quantitatively) based from the EDX spot analysis of representative As-vivianite particles (three particles for each sample, with at least six analysis spots *per* particle). The x_{AsO4} was calculated *per* spot as follows:

$$x_{AsO_4} = \frac{As_{at.\,\%}}{As_{at.\,\%} + P_{at.\,\%}} \quad \text{(eq. S-3)}$$

where: $As_{at.\,\%}$ atomic ratio of As;
$P_{at.\,\%}$ atomic ratio of P.

The x_{AsO4} was calculated and then averaged *per* particle, which was then used to get the mean value of x_{AsO4} from the three representative As-vivianite particle.

LCF analysis of Fe-K edge EXAFS. The x_{AsO4} in As-vivianites was estimated using linear combination fitting (LCF) analysis of the k^3-weighted Fe K-edge EXAFS spectra of the samples. LCF analyses were performed with SIXpack software over the *k*-range of 2 to 12.5 $Å^{-1}$ using the spectra of the end-members parasymplesite and vivianite.

PCA analysis of IR spectra. Principal component analysis (PCA) (Vandeginste *et al.*, 1998) was used to determine x_{AsO4} in the vivianite samples. PCA was performed using an in-house code written in Igor Pro v. 8.04. All IR spectra were normalized to total area of 1 before analysis.

Supplementary Tables

Table S-1 ICP-OES data for quality control solutions (QC) that were prepared from single element standard solutions (Merck Certipur®) to achieve chemical compositions similar to the experimental sample solutions. The mean results of *n* replicate analyses are given together with the standard deviation (s.d.) and relative standard deviation (RSD) (s.d. represents 68 % of the population, 2 s.d. represents 95 % of the population). The measured deviation from the reference value is a quantitative estimation of accuracy.

	As (mg L^{-1})	P (mg L^{-1})	Fe (mg L^{-1})
Wavelength (nm)	193.696	214.914	261.382
Instrumental limits			
Limit of detection (LoD)	0.011	0.022	0.012
Limit of quantification (LoQ)	0.032	0.048	0.022
Quality control			
QC verify (n = 6)			
Mean	0.327	2.17	4.26
s.d.	0.007	0.06	0.07
RSD	2.21 %	2.63 %	1.75 %
2RSD	4.42 %	5.27 %	3.50 %
Reference value	0.310	2.04	4.08
Measured deviation from reference value	5.74 %	6.05 %	4.39 %

Table S-2 Mineral saturation indices of vivianite, parasymplesite, amorphous $Fe(OH)_2$ and crystalline $Fe(OH)_2$ based on the elemental composition of the starting solutions used in the precipitation experiments.

Mole fraction AsO_4^{3-}	Concentration (mM)			Saturation indices			
	Fe^{2+}	PO_4^{3-}	AsO_4^{3-}	Vivianite	Parasymplesite	$Fe(OH)_2$, am.	$Fe(OH)_2$, cryst.
0	12.9	9.04	<0.01	10.8	-	-1.93	-1.34
0.22	13.1	6.39	2.11	10.7	9.80	-1.87	-1.27
0.48	12.8	4.02	4.02	10.4	10.6	-1.79	-1.19
0.71	13.1	2.09	6.32	9.94	11.2	-1.72	-1.12
0.82	12.7	1.37	6.67	9.59	11.2	-1.71	-1.11
0.90	12.9	0.74	7.44	9.09	11.4	-1.68	-1.08
0.95	12.3	0.38	7.37	8.51	11.4	-1.69	-1.09
1	13.1	<0.06	8.17	-	11.6	-1.66	-1.06

Table S-3 Elemental concentration (mM) and removal efficiencies (%) of Fe, P and As in the aqueous phase during aging of the mineral suspensions.

Mole fraction AsO_4^3	P				As				Fe			
	Conc. (mM)		Removal (%)		Conc. (mM)		Removal (%)		Conc. (mM)		Removal (%)	
	1 h	24 h	1 h	24 h	1 h	24 h	1 h	24 h	1 h	24 h	1 h	24 h
0	0.249	0.257	97.2	97.1	<0.002	<0.002	-	-	0.93	0.98	92.8	92.6
0.22	0.021	0.027	99.7	99.7	0.004	0.010	99.8	99.6	0.55	0.55	95.8	96.7
0.48	0.016	0.024	99.6	99.4	0.003	0.028	99.9	99.3	0.58	0.56	95.5	95.6
0.71	0.003	0.010	99.7	99.5	0.012	0.033	99.8	99.5	0.64	0.63	95.1	95.3
0.82	0.005	0.015	99.6	98.9	0.005	0.159	99.9	97.7	0.59	0.66	95.3	94.8
0.90	0.001	0.020	99.2	97.3	0.011	0.137	99.8	98.2	0.83	0.89	93.6	93.0
0.95	0.001	0.002	98.4	99.4	0.012	0.030	99.8	99.6	0.68	0.69	94.5	94.5
1	<0.001	<0.001	-	-	0.446	0.781	94.5	90.3	2.55	2.14	80.5	83.2

Table S-4 Mole fraction (x) of As-substitution in vivianite samples. Calculated standard errors are in parenthesis.

Nominal value	Calculated value				
	ICP-OES[a]	XRD[b]	SEM-EDX[c]	EXAFS[d]	IR-PCA[e]
0	-	-	-	-	-
0.25	0.22 (0.05)	0.19	-	0.29 (0.01)	0.22
0.50	0.48 (0.09)	0.43	0.37 (0.03)	0.49 (0.02)	0.44
0.75	0.71 (0.08)	0.63	-	-	0.68
0.83	0.82 (0.08)	0.81	-	-	0.77
0.91	0.90 (0.07)	0.82	-	0.93 (0.02)	0.85
0.95	0.95 (0.08)	0.84	0.97 (0.01)	-	0.92
1	-	-	-	-	-

Note: Calculated standard errors are based on the following: (a) analytical uncertainties based on repeat analysis (n = 8) of quality control solutions (see Table S-1); (b) Rietveld refinement analysis of the XRD data; (c) EDX quantification on from different spots (n = 6); (d) fit-derived errors from the linear combination (LCF) fitting analysis of the Fe K-edge EXAFS spectra of parasymplesite and vivianite (see Table 1 in main manuscript); and (e) PCA analysis of the IR spectra.

Table S-5 Refined lattice parameters of As-substituted vivianites (x = mole fraction of substituted AsO_4^{3-}) obtained from Rietveld analysis of the XRD patterns.

Sample	a (Å)	b (Å)	c (Å)	β (°)	Volume (Å^3)	R_{wp} (%)
Vivianite	10.0965	13.4466	4.7112	104.306	619.781	4.49
x = 0.22	10.1477	13.4723	4.7307	104.435	626.435	4.55
x = 0.48	10.2122	13.4895	4.7441	104.625	632.359	4.62
x = 0.71	10.2652	13.5305	4.7692	104.704	640.711	4.97
x = 0.82	10.2878	13.5497	4.7787	104.749	644.749	3.89
x = 0.90	10.3007	13.5550	4.7825	104.765	645.702	4.33
x = 0.95	10.3114	13.5581	4.7858	104.777	646.935	4.12
Parasymplesite	10.3204	13.5684	4.7887	104.806	648.306	6.44

Table S-6 LCF results and statistics of Fe K-edge k^3-weighted $\chi(k)$ EXAFS spectra of As-substituted vivianites. Fitting was done between 2 and 12.5 Å^{-1} using the spectra of the end-members.

AsO_4^{3-} substitution (mole fraction, *x*)	Weights		Sum	Red. χ2	R-factor
	Vivianite	Parasymplesite			
0.22	0.722 (0.014)	0.295 (0.014)	1.017	0.061	0.008
0.48	0.493 (0.019)	0.480 (0.020)	0.972	0.119	0.017
0.90	0.072 (0.019)	0.980 (0.020)	1.052	0.120	0.015

Table S-7 Summary of As K-edge EXAFS shell-by-shell fitting results of the As(V)-substituted vivianites (x = 0.22, 0.48, 0.90) and parasymplesite.

Sample	Atomic pairs	CN	*R* (Å)	σ^2 (Å^2)	ΔE_0 (eV)	R-factor
Parasymplesite	As-O	6.1 (0.6)	1.69 (0.01)	0.005 (0.001)	4.0 (1.5)	0.019
	As-O-O	*12*	1.82(R_{As-O}) = *3.07*	σ^2 (As-O)		
	As-Fe1	3.1 (0.7)	3.30 (0.02)	*0.004*		
	As-Fe2	2.4 (0.1)	3.46 (0.04)	σ^2 (As-Fe1)		
x = 0.22	As-O	5.3 (0.5)	1.69 (0.01)	0.004 (0.001)	4.6 (1.4)	0.018
	As-O-O	*12*	1.82(R_{As-O}) = *3.08*	σ^2 (As-O)		
	As-Fe1	3.0 (0.6)	3.31 (0.02)	*0.004*		
	As-Fe2	2.4 (0.7)	3.47 (0.03)	σ^2 (As-Fe1)		
x = 0.48	As-O	5.7 (0.6)	1.69 (0.01)	0.004 (0.001)	4.5 (1.5)	0.020
	As-O-O	*12*	1.82(R_{As-O}) = *3.08*	σ^2 (As-O)		
	As-Fe1	3.1 (0.7)	3.30 (0.02)	*0.004*		
	As-Fe2	2.4 (0.8)	3.47 (0.02)	σ^2 (As-Fe1)		
x = 0.90	As-O	5.3 (0.5)	1.69 (0.01)	0.002 (0.001)	4.7 (1.5)	0.018
	As-O-O	*12*	1.82(R_{As-O}) = *3.08*	σ^2 (As-O)		
	As-Fe1	3.2 (0.6)	3.30 (0.02)	*0.004*		
	As-Fe2	2.3 (0.8)	3.47 (0.02)	σ^2 (As-Fe1)		

Note: Variables included in the fit: CN, coordination number; *R*, interatomic distance; σ^2, mean-squared atomic displacement; and ΔE_0, change in threshold energy. Fitting parameters allowed to float are accompanied by fit-determined standard errors in parenthesis while constrained parameters appear in italics. The passive electron reduction factor (S_0^2) was fixed at 1.0. The multiple scattering As-O-O path was constrained geometrically to the single scattering As-O path (R_{As-O-O} = 1.82 × R_{As-O}). The σ^2(As-Fe) values were set to best value found empirically. All fits were carried out from 1 to 3.5 Å in $R + \Delta R$-space. The number of independent points (N_{IDP}) in the fits was 16.5 and the number of variables (N_{Var}) was 8.

Table S-8 IR bands assignments (cm^{-1}) of the As-substituted vivianites (x = mole fraction of substituted AsO_4) and their respective end-members.

Sample	Suggested band assignment					
	OH stretching	HOH bending	PO_4 stretching	AsO_4 stretching	H_2O libration	Outplane bends
Vivianite	3473, 3114	1665, 1614	1035, 966, 936	-	806	666
x = 0.22	3467, 3112	1665, 1615	1029, 967, 937	786	810	666
x = 0.48	3462, 3104	1665, 1615	1076, 1028, 970, 937	779	817	661
x = 0.71	3459, 3084	1665, 1618	1076, 1029, 980, 936	793, 773	816	654
x = 0.82	3459, 3084	1665, 1619	1076, 1036, 1024, 981, 935	794, 773	817	654
x = 0.90	3459, 3084	1663, 1619	1078, 1041, 1022, 981, 936	793, 772	817	651
x = 0.95	3459, 3082	1662, 1619	1043, 1021, 982	792, 770	816	651
Parasymplesite	3459, 3082	1661, 1620	-	792, 770	816	650

References used for band assignments: Nakamoto (1986), Socrates (2004), Frost *et al.* (2002, 2003), Myneni *et al.* (1998).

Supplementary Figures

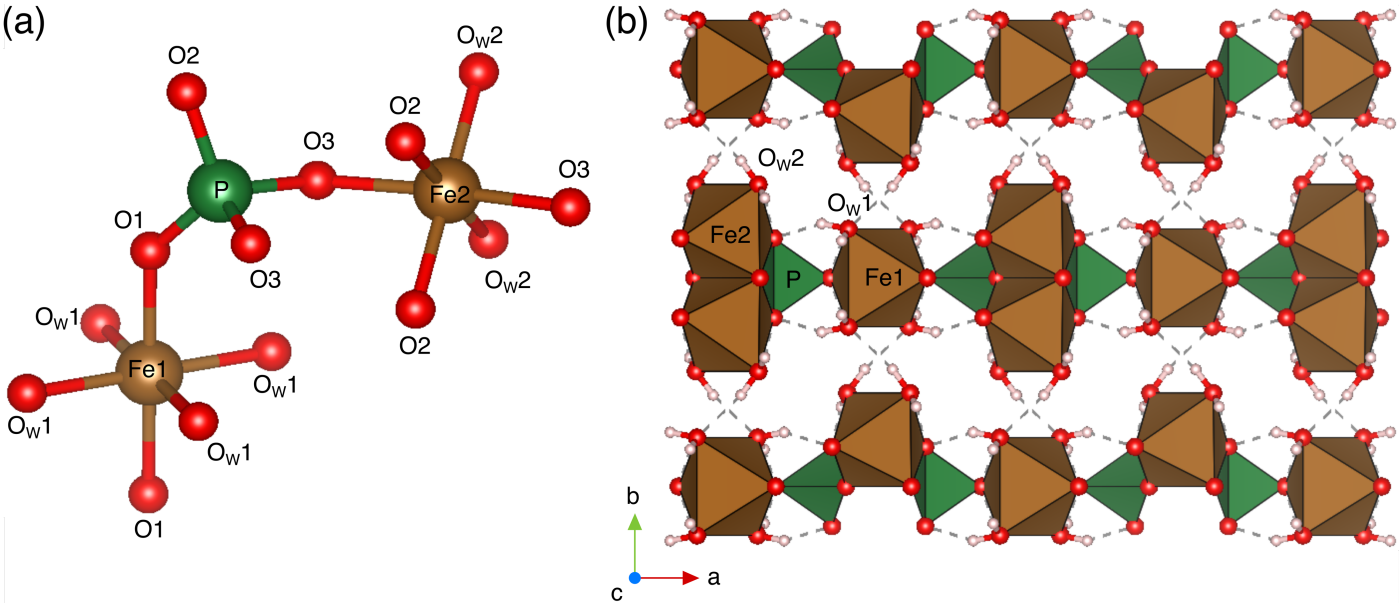

Figure S-1 **(a)** Coordination environment around the Fe1, Fe2 and P sites in the vivianite crystal. Hydrogen atoms were omitted for clarity. **(b)** Crystal structure of vivianite viewed in the *ab* plane showing layers of single Fe1 and edge-sharing Fe2 octahedra (brown) linked by phosphate tetrahedra (green). These layers are held together by hydrogen bonds (dashed lines). Oxygen and hydrogen atoms are indicated in red and pink, with O_w indicating oxygen atoms from water molecules. The local coordination environment and crystal structure were drawn using the VESTA software (Momma and Izumi, 2008) based on the crystallographic information by Capitelli *et al.* (2012).

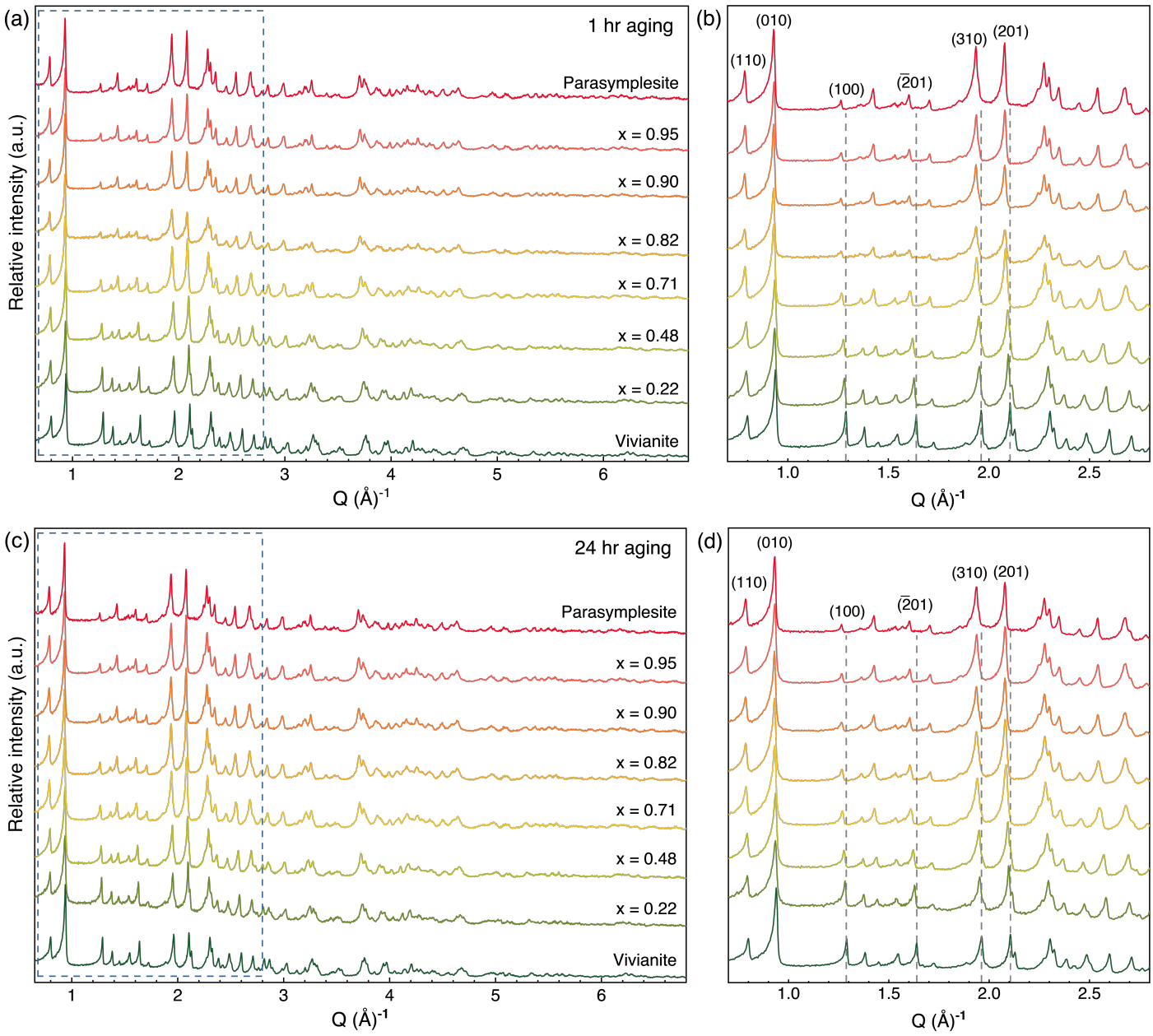

Figure S-2 **(a, c)** Full XRD patterns of the As-substituted vivianites (x = mole fraction of substituted AsO_4^{3-}) plotted in Q-space ($Q = 2\pi/d_{hkl}$) after aging for 1 and 24 h. **(b, d)** Enlarged XRD patterns from **(a)** and **(c)** as indicated by dashed rectangle. Dashed gray lines show the displacement in selected lattice planes in vivianite due to the substitution of AsO_4^{3-} for PO_4^{3-}.

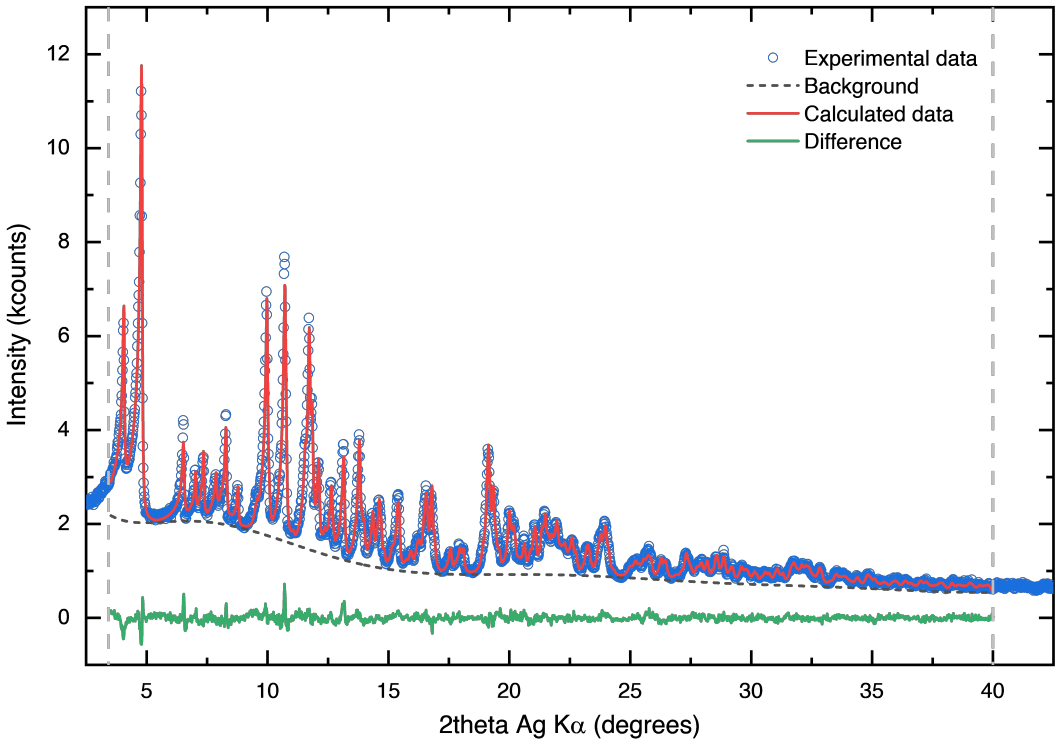

Figure S-3 Sample Rietveld refinement profile of As-substituted vivianite (x = 0.48). Refinement was performed using $C2/m$ vivianite and parasymplesite in the range of 3.5 to 40° 2θ (Ag Kα).

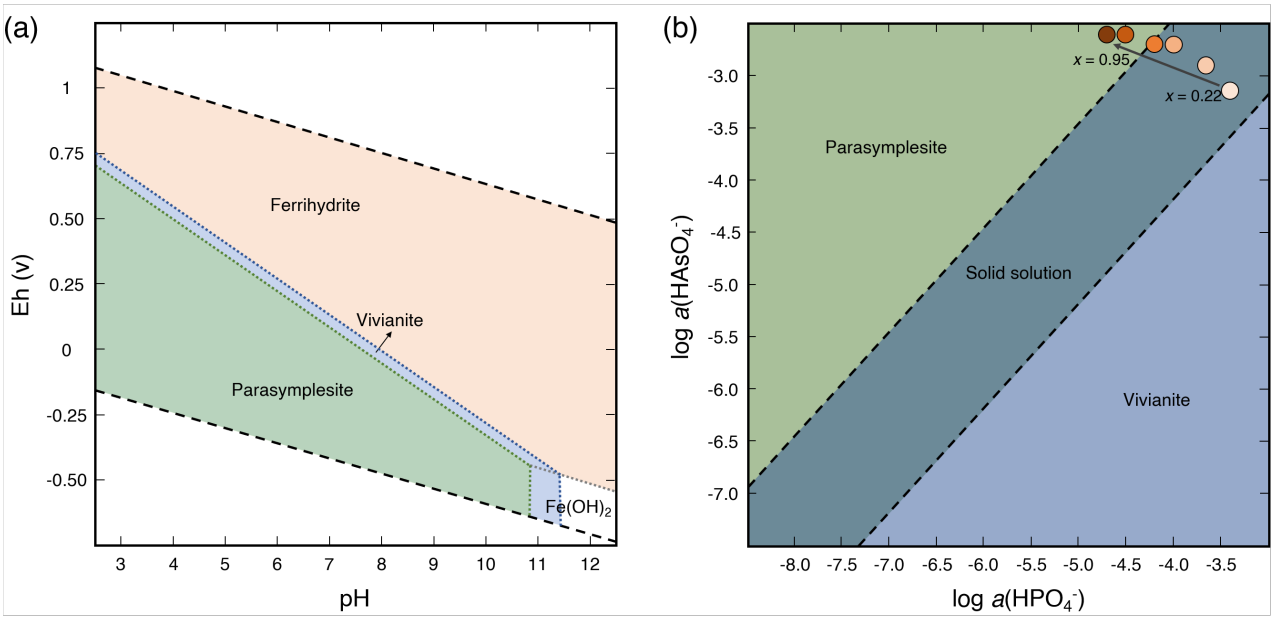

Figure S-4 Geochemical modelling results from Geochemist Workbench (Bethke, 2010) using the MINTEQ database: **(a)** Eh-pH diagram of the Fe-P-As-H_2O system at 25 °C which shows the overlap of the predominance fields of vivianite and parasymplesite and thus indicating a potential solid solution. **(b)** Mineral stabilities in the Fe-P-As-H_2O system at 25 °C. Coloured circles represent the As-substituted vivianites (x = mole fraction of substituted AsO_4^{3-}) synthesized in this study.

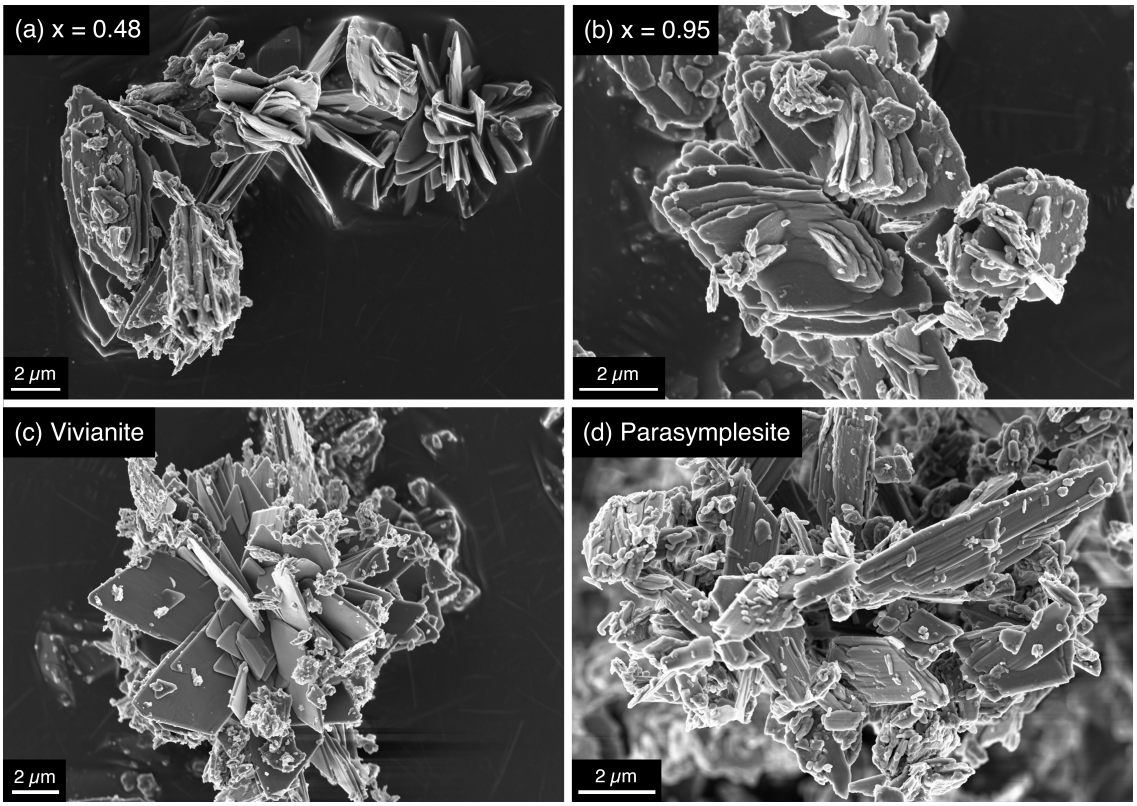

Figure S-5 SEM images of As-vivianites (x = mole fraction of substituted AsO_4^{3-}): **(a)** x = 0.48 and **(b)** x = 0.95, and the end-members **(c)** vivianite (x = 0) and **(d)** parasymplesite (x = 1).

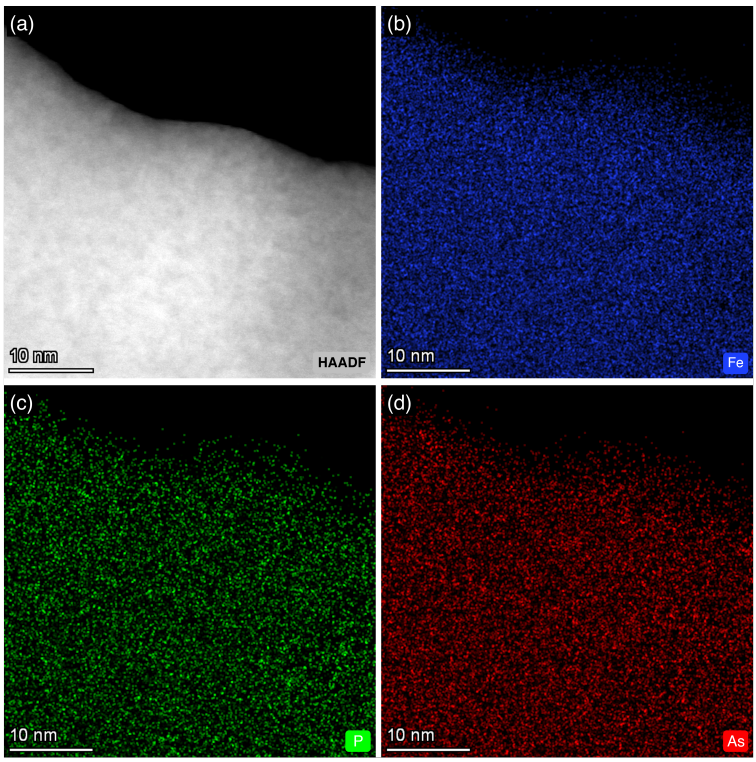

Figure S-6 **(a)** HAADF-STEM image of As-substituted vivianite (x = 0.48) and the corresponding EDX maps: **(b)** Fe (blue); **(c)** P (green); and **(d)** As (red).

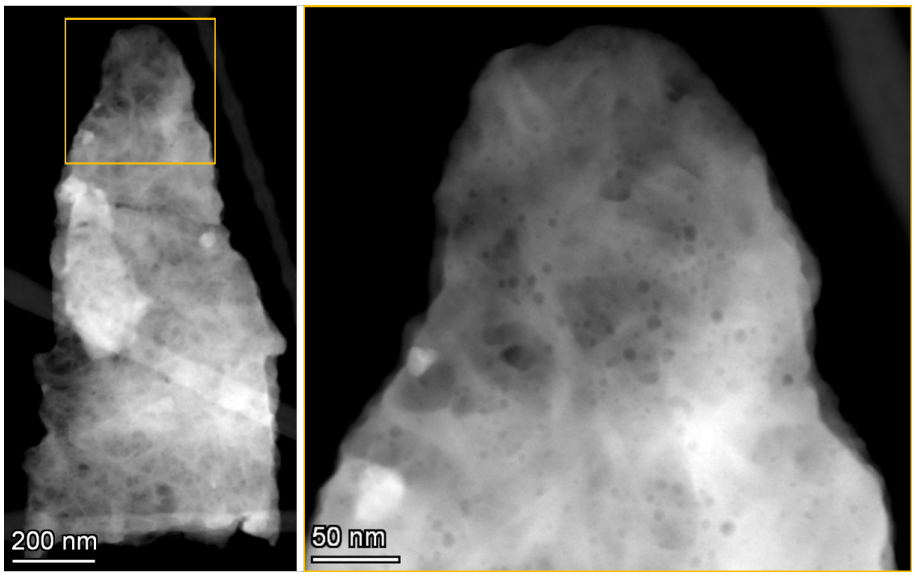

Figure S-7 **(Left)** HAADF-STEM image of As-substituted vivianite (x = 0.48) showing beam-induced changes in the crystal. **(Right)** Magnified HAADF-STEM image of the yellow marked area on the left.

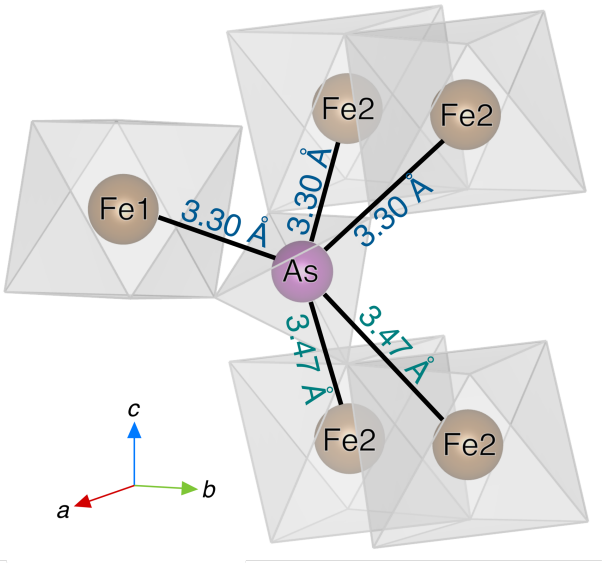

Figure S-8 Local bonding environment of tetrahedral AsO_4^{3-} around the Fe octahedra in parasymplesite showing the two As-Fe interatomic correlations: (i) CN = 3, R = 3.30 Å; and (ii) CN = 2, R = 3.47 Å.

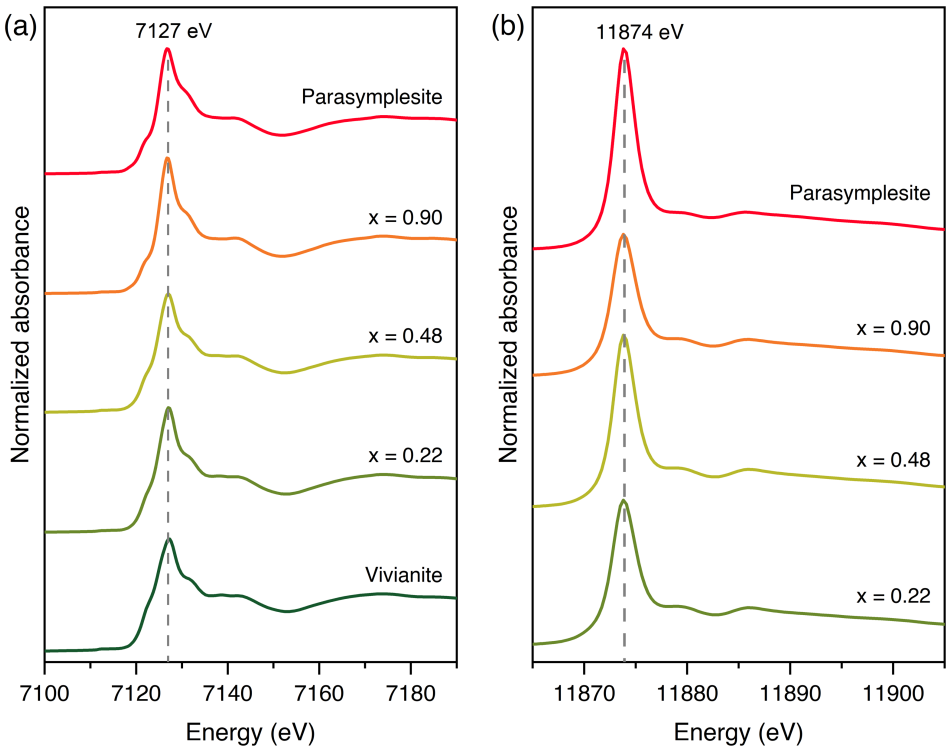

Figure S-9 **(a)** Fe and **(b)** As K-edge XANES spectra of the vivianite, parasymplesite and As(V)-substituted vivianites (x = 0.22, 0.48, 0.98).

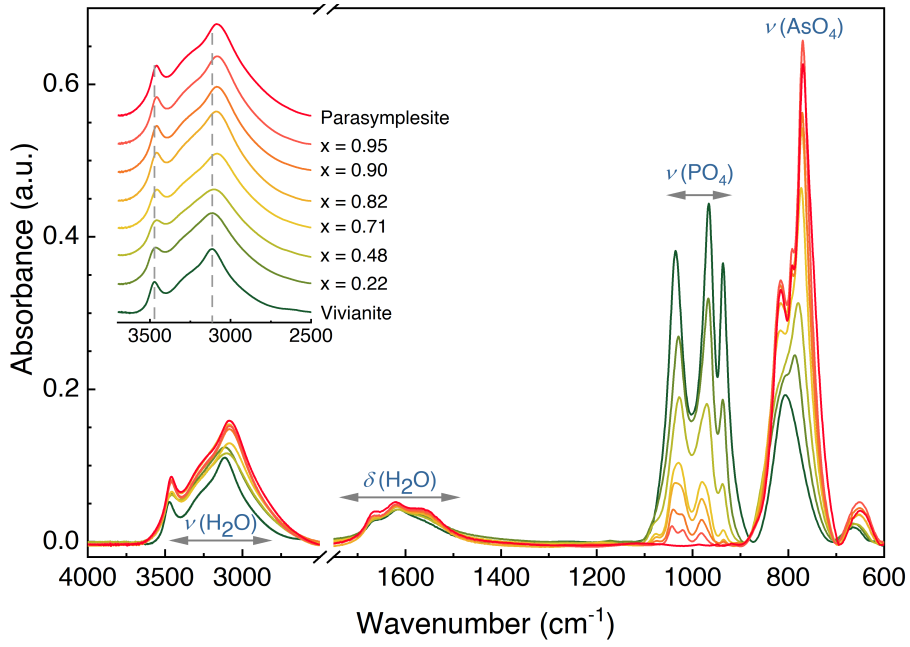

Figure S-10 IR absorption spectra of the As(V)-substituted vivianites (x = mole fraction of substituted AsO_4). Inset: Stacked spectra of the OH stretching region [ν(OH)] showing the positions of weakly and strongly hydrogen bonded H_2O at ~3400 and ~3100 cm^{-1}, respectively.

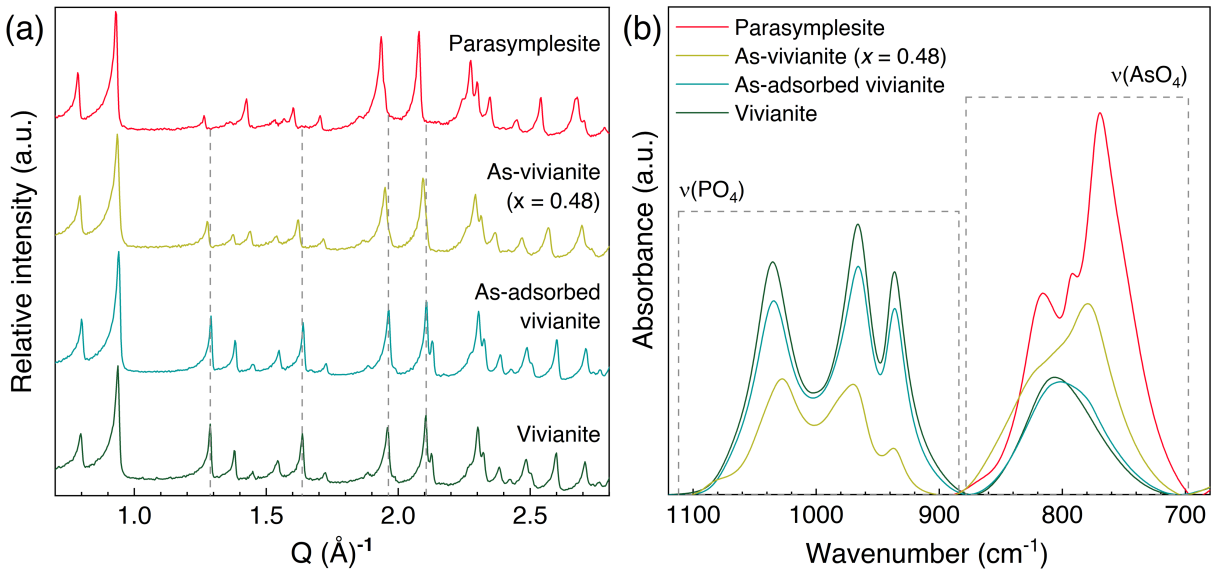

Figure S-11 Comparison between As-vivianite (*i.e.* structurally incorporated; $x = 0.48$), As-adsorbed vivianite (initial [As] = 4 mM, reaction time = 24 h) and the mineral end members vivianite and parasymplesite: **(a)** Zoomed XRD patterns in the Q-range of 0.7 to 2.8 Å. Dashed grey lines indicate vivianite reflections that represent lattice planes affected by As incorporation in vivianite. **(b)** FTIR spectra showing the clear difference in the $\nu(AsO_4)$ band of As-vivianite and As-adsorbed onto vivianite.

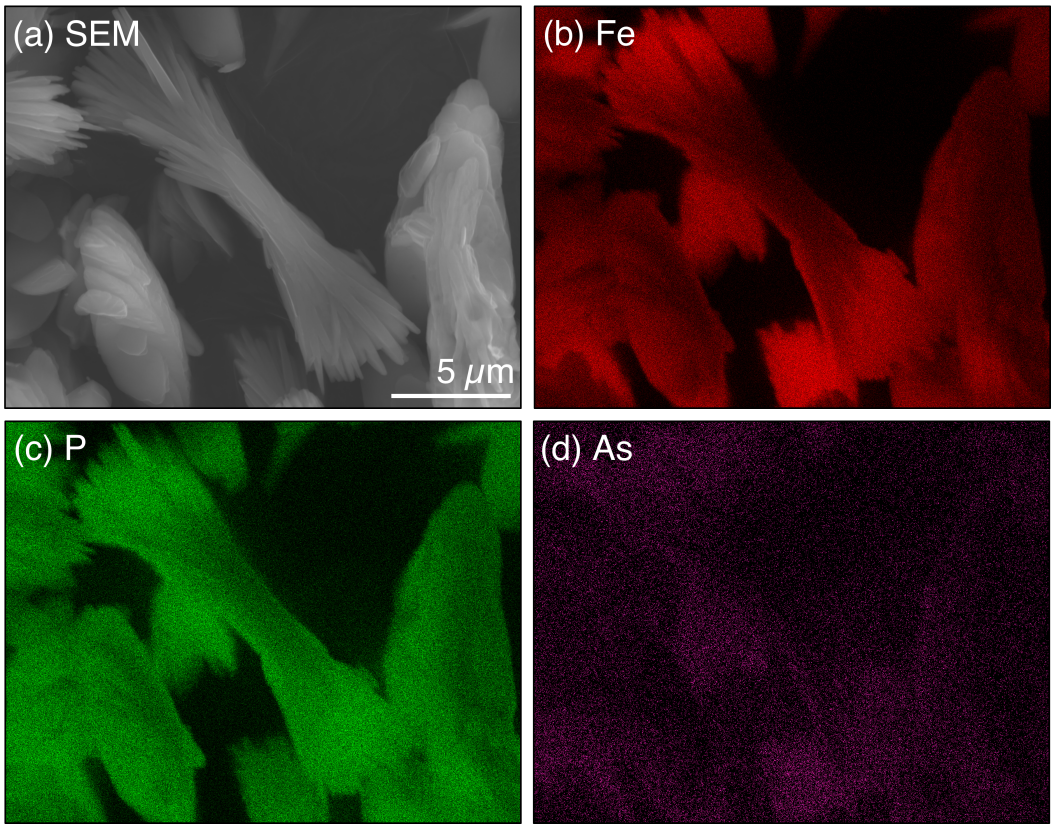

Figure S-12 **(a)** SEM image of pure vivianite ($[Fe]_{viv}$ = 12 mM) reacted with 4 mM As(V) at pH 7 for 24 h (comparable to the 48 mol % As-vivianite). The corresponding EDX maps of As-adsorbed vivianite: **(b)** Fe (red); **(c)** P (green); and **(d)** As (magenta).

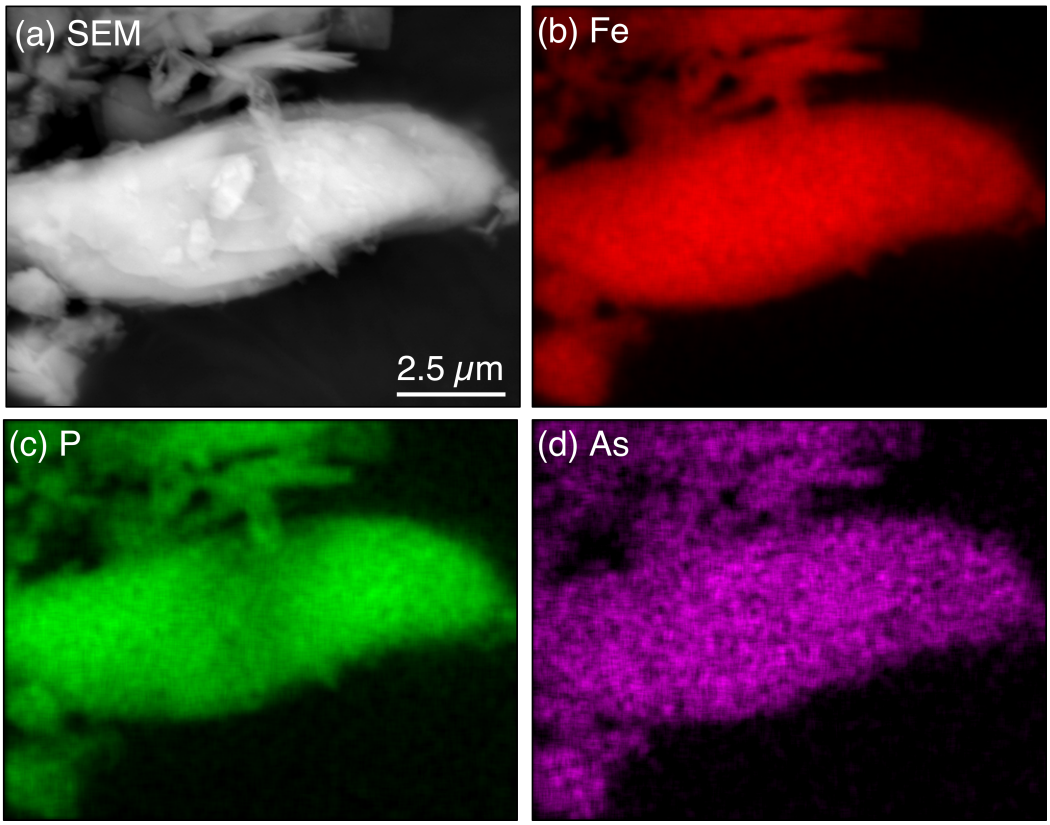

Figure S-13 **(a)** SEM image of 48 mol % As-vivianite and the corresponding EDX maps: **(b)** Fe (red); **(c)** P (green); and **(d)** As (magenta).

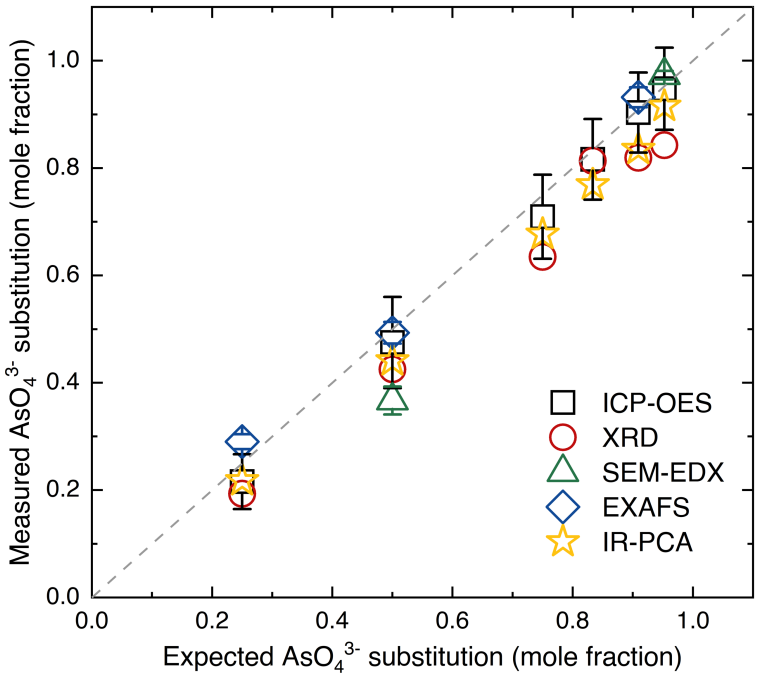

Figure S-14 Comparison of different characterization techniques used in this study for the quantification of As(V)-substitution in vivianite (see Text S-2.7 for more information). Error bars represent: (i) ICP, analytical uncertainties based on repeat analysis (n = 8) of quality control solutions (see Table S-4); (ii) XRD, Rietveld refinement analysis; (iii) SEM-EDX, quantification of different sample spots (n = 6) from representative particles (n = 3); (iv) EXAFS, LCF fit-derived errors (see Table S-6); and (v) PCA analysis of the IR spectra.

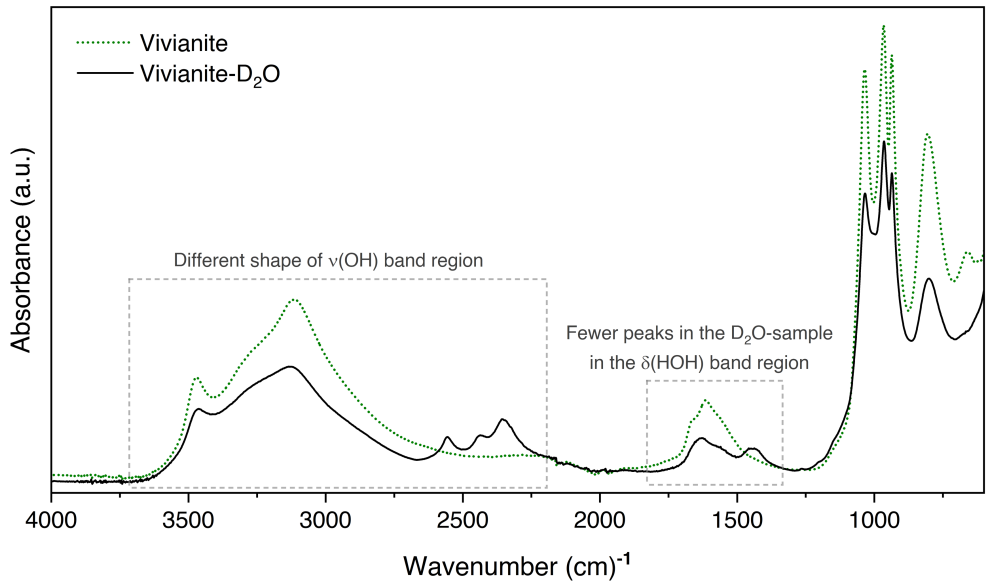

Figure S-15 IR spectra of vivianite and a partially deuterated vivianite. Vibrations involving hydrogen are shifted to lower wavenumbers.

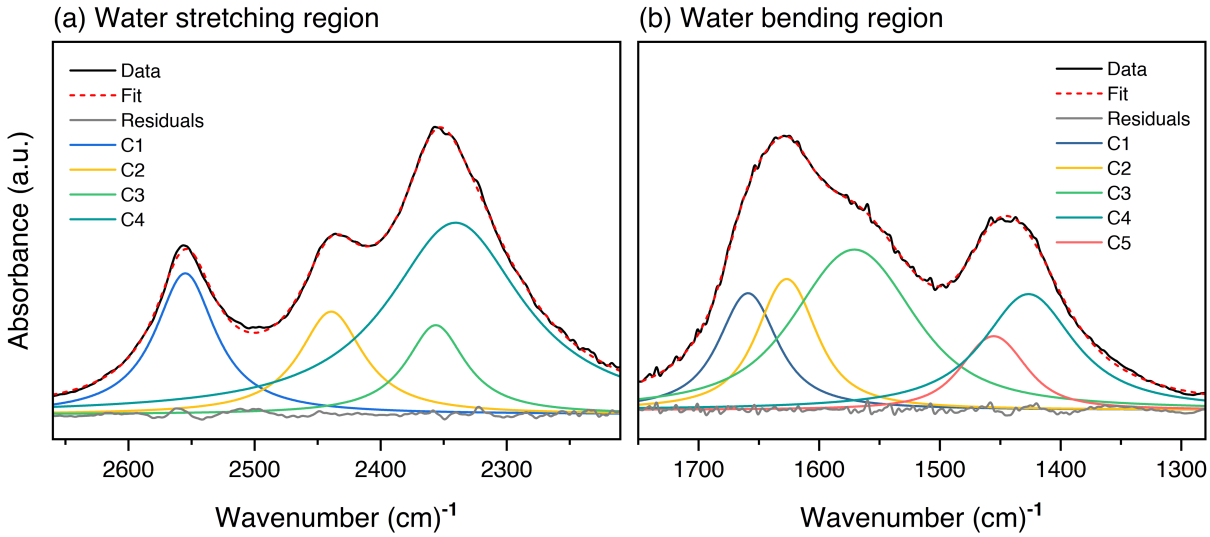

Figure S-16 **(a)** Deuterated water stretching region of partially deuterated vivianite. Only four Voigt curves are needed to achieve a good fit as expected for two distinct water bonding environments. **(b)** Bending region multi-Voigt fit of partially deuterated vivianite. Three peaks were used to fit the bending region of the protic and the two were used to fit the deuterated vivianite. Voigts 1, 2, 4 and 5 correspond to structural water bending modes. Voigt 3 may partially correspond to adsorbed water (wet sample); however, the enormous area disparity between Voigt 3 and other peaks indicate a very significant additional contribution to Voigt 3. This is interpreted to be the overtone of the water libration band at 804 cm^{-1} and not adsorbed or incorporated non-hydrogen bonded water as suggested by Frost *et al.* (2002).

Supplementary Information References

Al-Borno, A., Tomson, M.B. (1994) The temperature dependence of the solubility product constant of vivianite. *Geochimica et Cosmochimica Acta* 58, 5373–5378. https://doi.org/10.1016/0016-7037(94)90236-4

Bartl, H. (1989) Water of crystallization and its hydrogen-bonded crosslinking in vivianite $Fe_3(PO_4)_2 \cdot 8H_2O$; a neutron diffraction investigation. *Fresenius' Zeitschrift für analytische Chemie* 333, 401–403. https://doi.org/10.1007/BF00572335

Bethke, C.M. (2010) *Geochemical and Biogeochemical Reaction Modeling*. Cambridge University Press, Cambridge.

Capitelli, F., Chita, G., Ghiara, M.R., Rossi, M. (2012) Crystal-chemical investigation of $Fe_3(PO_4)_2 \cdot 8\ H_2O$ vivianite minerals. *Zeitschrift für Kristallographie - Crystalline Materials* 227, 92–101. https://doi.org/10.1524/zkri.2012.1442

Diaz-Moreno, S., Amboage, M., Basham, M., Boada, R., Bricknell, N.E., Cibin, G., Cobb, T.M., Filik, J., Freeman, A., Geraki, K., Gianolio, D., Hayama, S., Ignatyev, K., Keenan, L., Mikulska, I., Mosselmans, J.F.W., Mudd, J.J., Parry, S.A. (2018) The Spectroscopy Village at Diamond Light Source. *Journal of Synchrotron Radiation* 25, 998–1009. https://doi.org/10.1107/S1600577518006173

Frost, R.L., Martens, W., Williams, P.A., Kloprogge, J.T. (2002) Raman and infrared spectroscopic study of the vivianite-group phosphates vivianite, baricite and bobierrite. *Mineralogical Magazine* 66, 1063–1073. https://doi.org/10.1180/0026461026660077

Frost, R.L., Martens, W., Williams, P.A., Kloprogge, J.T. (2003) Raman spectroscopic study of the vivianite arsenate minerals. *Journal of Raman Spectroscopy* 34, 751–759. https://doi.org/10.1002/jrs.1049

Johnston, R.B., Singer, P.C. (2007) Solubility of Symplesite (Ferrous Arsenate): Implications for Reduced Groundwaters and Other Geochemical Environments. *Soil Science Society of America Journal* 71, 101–107. https://doi.org/10.2136/sssaj2006.0023

Kelly, S.D., Hesterberg, D., Ravel, B. (2008) Analysis of soils and minerals using X-ray absorption spectroscopy. In: Ulery, A.L., Drees, L.R. (Eds.) *Methods of Soil Analysis Part 5—Mineralogical methods*. Soil Science Society of America, Madison, WI, 387–463. https://doi.org/10.2136/sssabookser5.5.c14

Kitahama, K., Kiriyama, R., Baba, Y. (1975) Refinement of the crystal structure of scorodite. *Acta Crystallographica Section B: Structural Crystallography and Crystal Chemistry* 31, 322–324. https://doi.org/10.1107/S056774087500266X

Klementiev, K., Chernikov, R. (2016) XAFSmass: A program for calculating the optimal mass of XAFS samples. *Journal of Physics: Conference Series* 712, 012008. https://doi.org/10.1088/1742-6596/712/1/012008

Mikutta, C., Frommer, J., Voegelin, A., Kaegi, R., Kretzschmar, R. (2010) Effect of citrate on the local Fe coordination in ferrihydrite, arsenate binding, and ternary arsenate complex formation. *Geochimica et Cosmochimica Acta* 74, 5574–5592. https://doi.org/10.1016/j.gca.2010.06.024

Momma, K., Izumi, F. (2008) *VESTA*: A three-dimensional visualization system for electronic and structural analysis. *Journal of Applied Crystallography* 41, 653–658. https://doi.org/10.1107/S0021889808012016

Mori, H., Ito, T. (1950) The Structure of Vivianite and Symplesite. *Acta Crystallographica* 3, 1–6. https://doi.org/10.1107/S0365110X5000001X

Muehe, E.M., Morin, G., Scheer, L., Le Pape, P., Esteve, I., Daus, B., Kappler, A. (2016) Arsenic(V) Incorporation in Vivianite during Microbial Reduction of Arsenic(V)-Bearing Biogenic Fe(III) (Oxyhydr)oxides. *Environmental Science & Technology* 50, 2281–2291. https://doi.org/10.1021/acs.est.5b04625

Myneni, S.C.B., Traina, S.J., Waychunas, G.A., Logan, T.J. (1998) Experimental and theoretical vibrational spectroscopic evaluation of arsenate coordination in aqueous solutions, solids, and at mineral-water interfaces. *Geochimica et Cosmochimica Acta* 62, 3285–3300. https://doi.org/10.1016/S0016-7037(98)00222-1

Nakamoto, K. (1986) *Infrared and Raman Spectra of Inorganic and Coordination Compounds*. Wiley, Hoboken, NJ.

Newville, M. (2001) *IFEFFIT*: Interactive XAFS analysis and *FEFF* fitting. *Journal of Synchrotron Radiation* 8, 322–324. https://doi.org/10.1107/S0909049500016964

Paktunc, D., Dutrizac, J., Gertsman, V. (2008) Synthesis and phase transformations involving scorodite, ferric arsenate and arsenical ferrihydrite: Implications for arsenic mobility. *Geochimica et Cosmochimica Acta* 72, 2649–2672. https://doi.org/10.1016/j.gca.2008.03.012

Perez, J.P.H., Freeman, H.M., Schuessler, J.A., Benning, L.G. (2019) The interfacial reactivity of arsenic species with green rust sulfate (GR_{SO4}). *Science of The Total Environment* 648, 1161–1170. https://doi.org/10.1016/j.scitotenv.2018.08.163

Ratajczak, H., Yaremko, A.M. (2000) Theory of profiles of hydrogen stretching infrared bands of hydrogen-bonded solids. Multi-Fermi resonance effects and strong coupling between the high-frequency hydrogen stretching vibration and low-frequency phonons. *Journal of Molecular Structure: THEOCHEM* 500, 413–419. https://doi.org/10.1016/S0166-1280(00)00450-4

Rehr, J.J., Albers, R.C., Zabinsky, S.I. (1992) High-order multiple-scattering calculations of X-ray-absorption fine structure. *Physical Review Letters* 69, 3397–3400. https://doi.org/10.1103/PhysRevLett.69.3397

Socrates, G. (2004) *Infrared and Raman Characteristic Group Frequencies: Tables and Charts*. Third Edition, Wiley, Hoboken, NJ.

Šoptrajanov, B., Jovanovski, G., Pejov, L. (2002) Very low H–O–H bending frequencies. III. Fourier transform infrared study of cobalt potassium phosphate monohydrate and manganese potassium phosphate monohydrate. *Journal of Molecular Structure* 613, 47–54. https://doi.org/10.1016/S0022-2860(02)00130-8

Toby, B.H., Von Dreele, R.B. (2013) *GSAS-II*: The genesis of a modern open-source all purpose crystallography software package. *Journal of Applied Crystallography* 46, 544–549. https://doi.org/10.1107/S0021889813003531

Vandeginste, B.G.M., Massart, D.L., Buydens, L.M.C., De Jong, S., Lewi, P.J., Smeyers-Verbeke, J. (1998) Analysis of Measurement Tables. In: Vandeginste, B.G.M., Massart, D.L., Buydens, L.M.C., De Jong, S., Lewi, P.J., Smeyers-Verbeke, J. (Eds.) *Handbook of Chemometrics and Qualimetrics: Part B*. Elsevier, Amsterdam, 88–104. https://doi.org/10.1016/S0922-3487(98)80041-5

Webb, S.M. (2005) SIXpack: a graphical user interface for XAS analysis using IFEFFIT. *Physica Scripta* 2005, 1011–1014. https://doi.org/10.1238/Physica.Topical.115a01011